33. High Strain Rate and Impact Experiments

K. T. Ramesh

Experimental techniques for high-strain-rate measurements and for the study of impact-related problems are described. An approach to classifying these experimental techniques is presented, and the state-of-the-art is briefly described. An in-depth description of the basis for high-strain-rate experiments is presented, with an emphasis on the development of a range of strain rates and a range of stress states. The issues associated with testing metals, ceramics and soft materials are reviewed. Next, experimental techniques that focus on studying the propagation of waves are considered, including plate impact and shock experiments. Experiments that focus on the development of dynamic failure processes are separately reviewed, including experiments for studying spallation and dynamic fracture.

From a mechanics viewpoint, the consequences of an impact are threefold. First, stress waves or shock waves are propagated inside the impacted bodies, and the propagation of these waves must be understood. Second, large inelastic deformations might be developed, typically at high rates of deformation. Third, the entire impacted structure might be excited by the impact, leading to structural dynamics and vibration problems, typically at long times. This chapter explicitly ignores the last of these consequences. Further, if the impact velocity is sufficiently small, all of the stress waves propagated inside the impacted bodies will be elastic. The measurement of elastic wave propagation is discussed in other chapters, notably those on ultrasonics and photoacoustic characterization. Thus, our focus is on the experimental techniques associated with the propagation of nonelastic waves, and with the measurement of high-strain-rate behavior. Our emphasis is therefore on the measurement of the phenomena that are developed during the early times after a relatively high velocity impact.

It is useful to develop a sense of the range of strain rates developed during typical impact problems (note that the strain rates developed as a result of an impact are always functions of time, and therefore we focus here on the peak strain rates developed). Thus during an asteroid impact on the Earth, the peak strain rates that are developed are likely to be of the order of $10^8\,\mathrm{s}^{-1}$ (this results from hypervelocity impact, i. e. impact velocities above 5 km/s). For impacts corresponding to typical velocities from defense-related terminal ballistics ($\approx 1-2$ km/s), the peak strain rates developed are of the order of $10^5\,\mathrm{s}^{-1}$ to $10^6\,\mathrm{s}^{-1}$. All strain rates below the peak strain rate are likely to be developed during the event at sufficiently long times, and their significance to the problem must be determined on a case-by-case basis. In both the planetary impact and ballistic impact cases, for example, substantial parts of

the deformation occur at lower strain rates (perhaps as low as $10^2\,s^{-1}$). Further, significant parts of the damage that occur as a result of these events might be a result of the lower strain rate deformations (depending on the damage growth kinetics). This is because the high-strain-rates are typically sustained for much longer times than the ultra-high-strain-rates, and it takes time for many damage mechanisms (for example, the nucleation and growth of voids) to develop.

Experimental techniques that are colloquially defined as impact experiments can have dramatically different objectives. Since the design of the experimental technique is critically influenced by the final objective of the experiment, it is important to first decide what information one wishes to extract from the experiment. Typically, what are commonly called *impact* experiments fall into one of four different categories in order of increasing complexity in terms of the dynamics.

- *High-strain-rate experiments,* that is, experiments designed to measure the high-strain-rate properties of a material.
- *Wave-propagation experiments,* that is, experiments designed to understand the characteristics of wave propagation within the material or structure; these may develop high strain rates as well, but the high rate deformations vary in both space and time.
- *Dynamic failure experiments,* that is, experiments designed to understand the processes of dynamic failure within a material or structure.
- *Direct impact experiments,* that is, experiments designed to understand or discover broad impact phenomena (such as cratering efficiency experiments or vehicle crash experiments).

We now examine each of these types of experiments in detail.

33.1 High Strain Rate Experiments

One of the defining features of impacts that occur at velocities sufficiently large to cause inelastic (and particularly plastic) deformations is that most of these deformations occur at high strain-rates. These deformations may also lead to large strains and high temperatures. Unfortunately, we do not understand the high-strain-rate behavior of many materials (often defined as the dependence $\sigma_f(\varepsilon, \dot{\varepsilon}, T)$ of the flow stress on the strain, strain rate and temperature), and this is particularly true at high strains and high temperatures. A number of experimental techniques have therefore been developed to measure the properties of materials at high strain-rates. In this section we focus on those experimental techniques that develop controlled high rates of deformation in the bulk of the specimen, rather than those in which high-strain-rates are developed just behind a propagating wave front.

The primary experimental techniques associated with the measurement of the rate dependent properties of materials are described in Fig. 33.1 (note that the stress states developed within the various techniques are not necessarily identical). An excellent and relatively recent review of these methods is presented by *Field* et al. [33.1]. For the purposes of this discussion, strain rates above $10^2\,s^{-1}$ are classified as high strain rates, strain rates above $10^4\,s^{-1}$ are called very high strain rates, and strain rates above $10^6\,s^{-1}$ are called ultra highstrainrates. Conventionally, strain rates at or below $10^{-3}\,s^{-1}$ are considered to represent *quasistatic* deformations, and strain rates below $10^{-6}\,s^{-1}$ are considered to be in the *creep* domain.

Creep experiments are typically performed at relatively high temperatures, and a variety of specialized machines exist for these kinds of loading; dead loads are often of particular interest. Quasi static experiments are typically accomplished through a variety of servohydraulic machines, and ASTM standards exist for

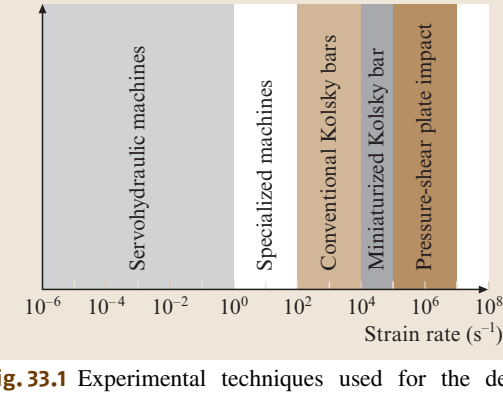

Fig. 33.1 Experimental techniques used for the development of controlled high strain rate deformations in materials

most of these experiments. Most servohydraulic machines are unable to develop strain rates larger than $10^0\,s^{-1}$ repeatably, but some specialized servohydraulic machines can achieve strain rates of $10^1\,s^{-1}$. Finally, the strain rates in the *intermediate rate* domain (between $10^0\,s^{-1}$ and $10^2\,s^{-1}$) are extremely difficult to study, since this is a domain in which wave-propagation is relevant and cannot be easily accounted for (however, the strain rates in this domain are indeed of interest to a number of machining problems). The primary approach to testing in this strain rate range uses drop towers or dropweight machines [33.2], and great care must be exercised in interpreting the data because of the coupling between impact-induced wave propagation and machine vibrations [33.3–7]. There are existing ASTM standards for some drop-weight tests, including ASTM E208-95a (2000) for measuring the ductility transition temperature of steels, ASTM E436-03 for performing drop-weight tear testing of steels and ASTM E680-79 (1999) for measuring the impact sensitivity of solid phase hazardous materials.

In this section we focus on experimental techniques for the higher strain rates (greater than $10^2\,s^{-1}$), including the high (10^2–$10^4\,s^{-1}$), very high (10^4–$10^6\,s^{-1}$) and ultra-high-strain-rate ($> 10^6\,s^{-1}$) domains.

33.1.1 Split–Hopkinson or Kolsky Bars

The now-classical experimental technique in the high-strain-rate domain is the Kolsky bar or Split-Hopkinson pressure bar (SHPB) experiment for determining the mechanical properties of various materials (e.g. [33.8–11] in metals, ceramics and polymers respectively) in the strain rate range of 10^{+2}–$8\times10^{+3}\,s^{-1}$. The terms *Split-Hopkinson pressure bar* and Kolsky bar are often used interchangeably. However, one should note that the term *Split-Hopkinson pressure bar* implies the performance of compression experiments, whereas the term *Kolsky bar* is more general and may include compression, tension, torsion or combinations of all of these. Since the fundamental concept involved in this technique – that of determining the dynamic properties of materials using two long bars as transducers, with the specimen size much smaller than the pulse length – was developed by *Kolsky* [33.12], we will use the term Kolsky bar in the rest of this chapter.

We begin by describing the compression Kolsky bar (an extensive description is presented in [33.13]). A schematic of the typical experimental apparatus is shown in Fig. 33.2. The device consists of two long bars (called the input and output bars) that are designed to remain elastic throughout the test. These bars sandwich a small specimen (usually cylindrical), which is expected to develop inelastic deformations. The bars are typically made of high-strength steels such as maraging steel, with a very high yield strength and substantial toughness. Other bar materials that have been used include 7075-T6 aluminum, magnesium alloys and PMMA (for testing very soft materials) and tungsten carbide (for testing ceramics). One end of the input bar is impacted by a projectile made of a material identical to that of the bars; the resulting compressive pulse propagates down the input bar to the specimen. The wave propagation is shown in the Lagrangian wave propagation diagram of Fig. 33.3, where time $t = 0$ corresponds to the instant of projectile impact. Several reverberations of the loading wave occur within the specimen; a transmitted pulse is sent into the output bar and a reflected pulse is sent back into the input bar. Typically, resistance strain gages are placed on the input and output bars for measuring

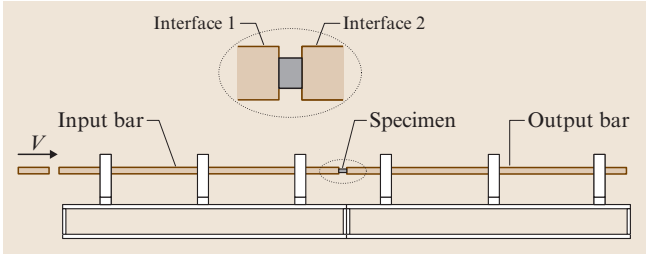

Fig. 33.2 Schematic of the compression Kolsky bar. The input and output bars are designed to remain elastic, as is the pacting projectile

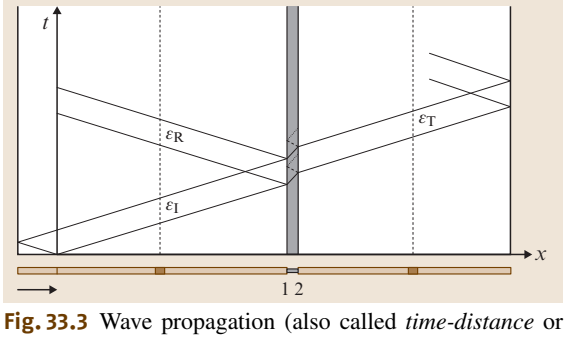

Fig. 33.3 Wave propagation (also called *time-distance* or *Langrangian*) diagram showing the stress waves progagating through space and time in the Kolsky bar arrangement. The strain gauge locations are also shown. Speciman length is exaggerated to show the wave reverberation in the specimen

1. the incident pulse generated by the impacting projectile,
2. the reflected pulse from the input bar/specimen interface and
3. the transmitted pulse through the specimen to the output bar.

Note that the strain gauge locations are ideally such that the incident and reflected pulses do not overlap, as shown in Fig. 33.3. The strain gage signals are typically measured using high-speed digital oscilloscopes with at least 10-bit accuracy and preferably with differential inputs to reduce noise.

Let the strain in the incident pulse be denoted by ε_I, that in the reflected pulse by ε_R, and that in the transmitted pulse by ε_T (these are bar strains as measured by the strain gages). Examples of the raw signals measured on the input and output bars are presented in Fig. 33.4 for a test on vanadium. Then the characteristic relations associated with one dimensional elastic wave propagation in the bar tell us that the particle velocity at the specimen/input-bar interface is given by

$$v_1(t) = c_b\left(\varepsilon_I - \varepsilon_R\right) , \tag{33.1}$$

and that at the specimen/output-bar interface is given by

$$v_2\,(t) = c_b \varepsilon_T , \tag{33.2}$$

where $c_b = \sqrt{(E_b)/(\rho_b)}$ is the bar wave speed, with E_b the Young's modulus and ρ_b the density of the bar material. The mean axial strain rate in the specimen is then given by

$$\dot{e}_s = \frac{v_1 - v_2}{l_0} = \frac{c_b}{l_0}\left(\varepsilon_I - \varepsilon_R - \varepsilon_T\right) , \tag{33.3}$$

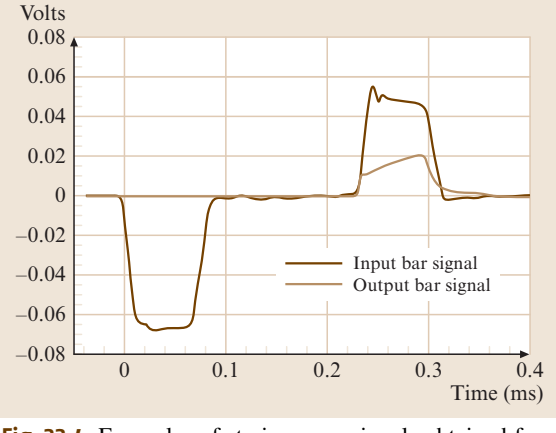

Fig. 33.4 Examples of strain gauge signals obtained from the input and output bars for a high strain rate test an pure vanadium tested at 600 °C

where l_0 is the initial specimen length. Since the strains in the elastic bars are known, we can then compute the bar stresses and thence the normal forces at the two specimen/bar interfaces as

$$P_1 = E_b\left(\varepsilon_I + \varepsilon_R\right) A_b \tag{33.4}$$

and

$$P_2 = E_b\left(\varepsilon_T\right) A_b \tag{33.5}$$

at the specimen/input-bar and specimen/output-bar interfaces respectively. The mean nominal axial stress $\bar{s}_s$ in the specimen is then given by

$$\bar{s}_s\,(t) = \frac{P_1 + P_2}{2}\frac{1}{A_{s0}} = \frac{E_b}{2}\frac{A_b}{A_{s0}}\left(\varepsilon_I + \varepsilon_R + \varepsilon_T\right) \tag{33.6}$$

where A_{s0} is the initial cross-section area of the specimen.

It is instructive to examine the wave propagation within the specimen in some detail (Fig. 33.3). When the incident pulse arrives at the specimen a compressive loading wave is generated inside the specimen. The compressive loading wave propagates through the specimen and arrives at the specimen output-bar interface. By design, the specimen's impedance is smaller than the impedance of the bars surrounding the specimen on both sides. Since the output bar has a higher impedance than the specimen itself, the wave that reflects from the specimen/output-bar interface remains a loading wave, resulting in an even higher compressive stress. This wave now arrives at the specimen/input-bar interface, again sees a higher impedance and again reflects as a loading wave, resulting in a further increase in the compressive stress. This process continues until the stress within the specimen reaches a value that is sufficiently high to generate inelastic strains, resulting in finite plastic flow of the specimen under the compressive loading. Once substantial plastic flow of the specimen material has commenced, we may neglect further wave propagation within the specimen, since the amplitude of the subsequent wavefronts will be very small. Thus at these later times the stress within the specimen is essentially uniform; the stress is said to have equilibrated. If the boundary conditions are frictionless, the specimen stress is also uniaxial.

Once an equilibrium condition has been achieved, we have $P_1 = P_2$, and (33.4) and (33.5) then imply that

$$\varepsilon_I + \varepsilon_R = \varepsilon_T . \tag{33.7}$$

This condition, together with (33.1), (33.2), (33.4) and (33.5), substantially simplifies equations (33.3) and

(33.6) for the specimen strain rate and specimen stress. That is, by assuming stress equilibrium, uniaxial stress conditions in the specimen and 1-D elastic stress wave propagation without dispersion in the bars (discussed et seq.), the nominal strain rate $\dot{e}_s$, nominal strain e_s and nominal stress s_s (all in the specimen) can be estimated using

$$\dot{e}_s(t) = -\frac{2c_b}{l_0}\varepsilon_R(t) \ , \tag{33.8}$$

$$e_s(t) = \int_0^t \dot{e}_s(\tau)\,\mathrm{d}\tau \ , \tag{33.9}$$

and

$$s_s(t) = \frac{E_b A_b}{A_s}\varepsilon_T(t) \ , \tag{33.10}$$

where A_s and l_0 are the initial cross-sectional area and length of the specimen respectively. Note the negative sign in (33.8). This arises because the strain in the reflected pulse has the opposite side of the strain in the incident pulse; the latter is compressive and is conventionally considered positive in these experiments. Thus the specimen strain rate expressed by equation (33.8) is a positive strain-rate, i. e., in this convention, a compressive strain-rate. The true strain and true strain rate in the specimen are then given by [33.14]

$$\varepsilon_s(t) = -\ln[1 - e_s(t)] \ , \tag{33.11}$$

and

$$\dot{\varepsilon}_s(t) = \frac{\dot{e}_s(t)}{1 - e_s(t)} \ . \tag{33.12}$$

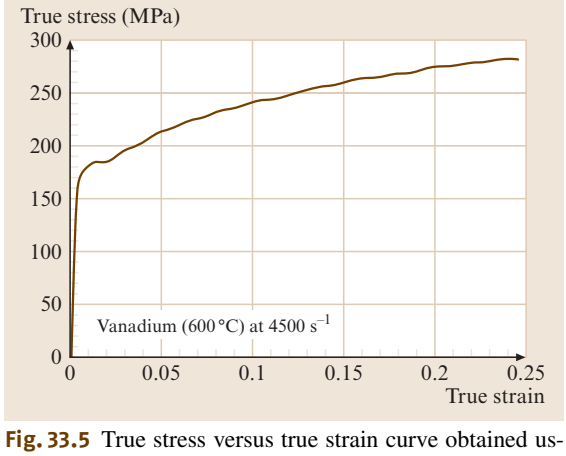

Fig. 33.5 True stress versus true strain curve obtained using the signals presented in Fig. 33.4. The material is vanadium tested at 600 °C at a strain rate of 4500 s^{-1}

Note that compression is defined as positive. Assuming plastic incompressibility, the true stress σ_s in the specimen is obtained as

$$\sigma_s(t) = s_s(t)\,[1 - e_s(t)] \ . \tag{33.13}$$

From (33.9) and (33.10), a stress-strain curve is obtained at a strain rate defined by an average taken over the strain rate history obtained in (33.8); an example of such a stress-strain curve is presented in Fig. 33.5 (obtained on vanadium using the pulses presented in Fig. 33.4). We note here that the correction to a true strain rate represented by (33.12) has often not been used by researchers in the field, resulting in the peculiar situation that papers will present true stress versus true strain curves obtained at an *engineering* (rather than *true*) strain-rate. The magnitude of this correction can be considerable is the final strain is of the order of 20%.

The Design of Kolsky Bar Experiments

The design of a specific Kolsky bar experiment essentially comes down to the design of the specimen (i. e., the choice of specimen length l_0 and diameter d_0) and the choice of the projectile impact velocity so as to attain a specific strain rate in the specimen. Other design parameters such as the bar length L and the bar diameter D are more relevant to the design of the Kolsky bar system rather than the specific experiment. The most important design parameters are the three ratios: L/D, D/d_0 and l_0/d_0. Typically, L/D is of order 100, D/d_0 is of order 2 to 4, and l_0/d_0 is 0.6 to 1. The choice of bar diameter itself depends on the material being tested, the typical specimen sizes that are available, and the degree of wave dispersion that is allowable. Although using a large value of D/d_0 provides a large area mismatch and thus allows for the testing of much harder specimen materials, the expectation that the specimen-bar interface can be approximated as a plane places limits on the value of this ratio (that is, one needs to avoid the punch problem). The majority of Kolsky bars in common use in the world are between 7 mm and 13 mm in diameter, although very large bar diameters have been used for experiments on concrete (e.g., [33.15]; very large bar diameters have a specific disadvantage in that launching the projectile may require substantial gun facilities).

A systematic way to perform experimental design is presented below. The strain in the incident pulse is given by

$$\varepsilon_I = \frac{V}{2c_b} \ , \tag{33.14}$$

where V is the projectile velocity. Using this and the equilibrium condition (33.7) in (33.10), we can write the

specimen stress entirely in terms of the reflected strain and the impact velocity:

$$s_s(t) = \frac{E_b A_b}{A_s}\varepsilon_T(t) = \frac{E_b A_b}{A_s}(\varepsilon_I + \varepsilon_R) = \frac{E_b A_b}{A_s}\left(\frac{V}{2c_b} + \varepsilon_R\right). \quad (33.15)$$

However, (33.8) allows us to write the strain in the reflected pulse in terms of the specimen strain rate

$$\varepsilon_R = -\frac{l_0}{2c_b}\dot{e}_s. \quad (33.16)$$

Using this in (33.15), we obtain the relation between the specimen stress and the specimen strain rate that must be satisfied during any given test using a specific Kolsky bar, a specific specimen, and a particular choice of impact velocity

$$s_s(t) = E_b\left(\frac{A_b}{A_s}\right)\left(\frac{V}{2c_b}\right) - E_b\left(\frac{A_b}{A_s}\right)\left(\frac{l_0}{2c_b}\right)\dot{e}_s. \quad (33.17)$$

This last result represents what we call a test characteristic response: that is, the constraints of the experimental configuration force any observed stresses and strain rates in the specimen to satisfy (33.17). The result is shown as the straight line in Fig. 33.6, which is a plot of the stress versus the strain-rate (hereafter called a *response diagram*). Note that in this figure compressive stresses are presented along the positive Y-axis, following a convention. The straight line in Fig. 33.6 represents the locus of all points in stress versus strain-rate space that can be reached using a compression Kolsky bar, a specific specimen geometry, and a specific projectile impact velocity. Figure 33.6 also shows the curve corresponding to the constitutive response of the specimen material (typically the flow stress increases with strain-rate). The stresses and strain rates actually observed in a given test correspond to the intersection of the test response line with the constitutive curve, as shown in Fig. 33.6. Given that the constitutive response of the material is not controllable, a specific strain-rate can only be achieved by moving the test response line; that is, in order to sample other points along the constitutive curve, we would need to move the straight line corresponding to the experimental parameters. Equation (33.17) indicates that the maximum strain rate that can be observed in a Kolsky bar test is given by

$$\dot{e}_s|_{max} = \frac{V}{l_0}, \quad (33.18)$$

while the maximum compressive stress that can be observed in such a test is given by

$$s_s|_{max} = E_b\left(\frac{A_b}{A_s}\right)\left(\frac{V}{2c_b}\right). \quad (33.19)$$

Figure 33.6 shows that the maximum strain rate can only be approached an actual Kolsky bar test if the material response is exceedingly soft, so that the observed specimen stress is very close to zero. Conversely, the maximum specimen stress can only be observed in the test if the specimen strain rate is very close to zero. This is a mathematical manifestation of the well-known result that a given test procedure will generate lower strain

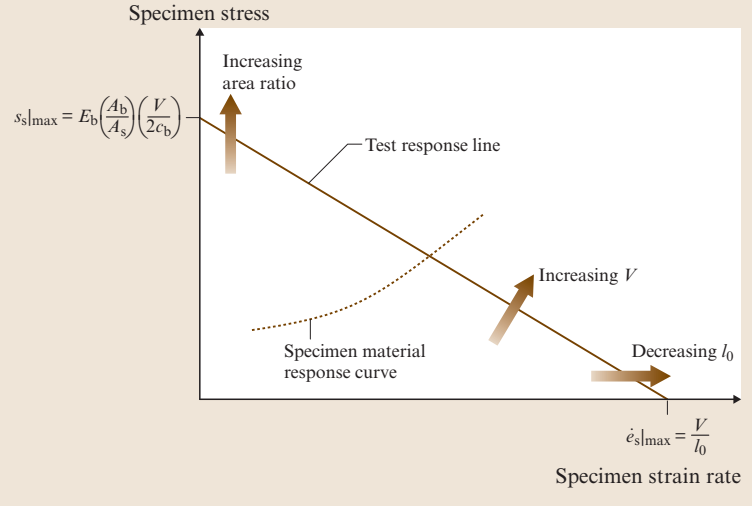

Fig. 33.6 Response diagramm for the compression Kolsky bar, showing the intersection of the material response curve (*dashed*) with the test response line

rates on strong materials, while very soft materials can be deformed at very high strain rates in an identical test. As Fig. 33.6 shows, it is apparent that the easiest way to get a higher maximum strain rate would be to increase the impact velocity or to reduce the specimen length. Similarly, an increase in the maximum observable stress (e.g. when studying very strong materials) can be obtained by increasing the impact velocity or by increasing the area mismatch A_b/A_s. However, these parameters cannot be varied arbitrarily; restrictions are usually imposed by the requirements for test validity (see, for example, *Jia* and *Ramesh* [33.16], outlined next. Other restrictions arise from such issues as the yielding of the bar material (which limits impact velocity) and the sensitivity of the strain gages and signal-to-noise ratio of instrumentation (which determines the smallest stresses that can be effectively measured).

Requirements for Valid Kolsky Bar Experiments

Several basic requirements must be satisfied in order to ensure that the measured response in a Kolsky bar experiment is truly the constitutive behavior of the specimen material. We discuss each of these requirements briefly below.

Equilibrated Stresses. The nature of the Kolsky bar experiment is such that the loading arrives first at one side of the specimen. Because stress waves propagate in the specimen at finite speeds, equilibration of the stresses takes a non-zero time. Equilibration of the stresses is required to ensure that the stress measured from the output bar side of the specimen represents the average stress in the specimen. In terms of experimental design, equilibration of the stresses will occur if the loading time of interest is long in comparison with the *specimen characteristic time* ($\tau_s = c_{sp}/l_0$, the time for the compressive wave to traverse the length of the specimen). *Davies* and *Hunter* estimated that three reverberations of the loading wave in the specimen are required for stress equilibration [33.17] for ductile metal specimens. The ability to check that the axial stress has in fact equilibrated at the time of interest is critical for the successful use of any Kolsky bar technique. The typical approach to checking equilibrium involves a comparison of the force histories on the two sides of the specimen [33.13]. Note that the axial stress distributions in the specimen cannot be measured in Kolsky bar experiments, since only the forces at the two ends of the specimen are experimentally accessible. For some situations (such as an experiment on a soft specimen material or at very high strain rates) even the force at the input-bar/specimen interface is difficult to obtain accurately, because the measure of this force involves a subtraction of two pulses with similar magnitudes that have suffered wave dispersion. For the more complex experiments, involving very soft specimens or extremely high-strain-rates, it is sometimes necessary to perform a full computational analysis of the wave propagation within the specimen to obtain an estimate of the time required for equilibration [33.16].

Friction Effects. Friction at the specimen/bar interfaces causes the state of stress to deviate from the uniaxial stress condition and leads to spuriously stiff results [33.18, 19]. As Fig. 33.5 shows, decreasing the specimen length can greatly increase the accessible strain rate range for a given experiment. However, as the l_0/d_0 ratio of the specimen becomes smaller, the effects of friction at the interfaces become substantial if the coefficient of friction at the specimen/bar interfaces is not sufficiently low, leading to inaccurate measures of the stress [33.19]. For quasi-static compression tests, specimen l_0/d_0 ratios of 1.5 to 3.0 are recommended in various ASTM standards [33.20], with proper use of lubricant. In contrast, for conventional compression Kolsky bar tests, l_0/d_0 ratios of 0.5–1.0 are widely used, following *Bertholf* and *Karnes* [33.19]. The interfacial friction depends on the smoothness of the end surfaces, the bar and specimen materials and lubricant used, impact velocity and temperature. Commonly used lubricants in Kolsky bar experiments include MoS_2 lubricants and lithium greases. Several researchers have measured the friction of lubricants at various strain rates using ring specimens (e.g. [33.21]). These measurements have generally shown that the friction decreases at high strain rates.

Dispersion Effects. Longitudinal waves in elastic bars suffer from geometric dispersion, so that the incident, reflected and transmitted pulses change as they propagate along the input and output bars; however, (33.1–33.13) essentially ignore dispersion. Wave dispersion affects the measured strain pulses, which in turn affect the measured stress-strain response. Dispersion effects can be rigorously included through elastic wave propagation computations (e.g. [33.22]), but two consequences of dispersion remain important. First, dispersion inevitably induces superimposed oscillations in the loading of the specimen. Second, shorter stress pulses with sharper rise times cause greater dispersion because of the high-frequency content and the wider

range. It is now possible to routinely correct for the effects of dispersion are using elastic-wave propagation calculations, and indeed this must be done for some experiments where information that is present early in the stress-time signal is important. One approach to minimizing the effects of dispersion is to use so-called buffer materials or shaper materials that are placed between the impacting projectile and input bar [33.23]. This results in the shaping of the incident wave with a longer rise time and thus lower dispersion.

Inertial Effects. The stresses associated with axial and radial inertia should be small compared with the flow stress of the material under investigation. The stress wave loading that is used in high strain rate experiments causes inertia to have an influence on the measured properties, particularly at very high strain rates [33.24]. The magnitude of the inertial contribution to the apparent stress also depends on the density and size of the specimen [33.16]. *Gorham* [33.24] (following [33.25]) developed an approach to estimate the inertial effect in Kolsky bar experiments that can be rewritten to emphasize specimen size and l/d ratio effects as follows:

$$\sigma_{s,2} - \sigma_y = \rho d^2 \dot{\varepsilon}^2 \left[\frac{1}{64} + \frac{1}{6} \left(\frac{l_0}{d_0} \right)^2 \right] - \rho d^2 \ddot{\varepsilon} \left[\frac{1}{32} - \frac{1}{6} \left(\frac{l_0}{d_0} \right)^2 \right] - \frac{\rho l \dot{v}}{2} , \tag{33.20}$$

where $\sigma_{s,2}$ and σ_y are the flow stress measured from the output bar and the actual yield stress of the material respectively, ρ is the density of the specimen material and v is the velocity of the interface between the specimen and the output bar. This rearrangement is useful because the l/d ratio is constrained to remain within a fairly narrow range ($0.5 \le l/d \le 1$), and so (33.20) allows us to focus on the effect of specimen size through the specimen diameter. In any experiment with a nearly constant strain rate, the magnitude of the second term is much smaller than that of the first term, and the magnitude of the third term is generally small for materials which do not exhibit a very high strain hardening. Ignoring the second and the third terms, the relative error (r) in flow stress measurement due to inertia is

$$\frac{\sigma_{s,2} - \sigma_y}{\sigma_y} = r = \frac{\rho d^2}{\sigma_y} \left[\frac{1}{64} + \frac{1}{6} \left(\frac{l_0}{d_0} \right)^2 \right] \dot{\varepsilon}^2 . \tag{33.21}$$

It is apparent that (for a given strain rate) the error drops significantly when the specimen size (length or diameter, given l_0/d_0 is reduced (this is one driver for miniaturizing the Kolsky bar arrangement). It is also apparent that tests on materials with high flow stress and low density are less prone to such inertial errors, whereas very high density materials and very soft materials will be problematic. A useful way to consider inertial effects is to examine the limiting strain rate that can be attained while keeping the inertial error below some chosen value. For a given value of the relative error $r$in stress and a given ratio of l_0/d_0, the limiting strain rate can be expressed as a function of the specimen length and the specific strength σ_y/ρ as

$$\dot{\varepsilon}_{\lim} = \frac{1}{l_0} \sqrt{\frac{\sigma_y}{\rho} r \left(\frac{192}{32 + \left(\frac{3}{\beta^2} \right)} \right)} , \tag{33.22}$$

where $\beta = (l_0)/(d_0)$.

This gives us, for example, $\dot{\varepsilon}_{\lim} = 1/l_0[(48r)/11]^{1/2}[(\sigma_y)/(\rho)]^{1/2}$ when $\beta = l_0/d_0$ is assumed to be 0.5. Figure 33.7 shows this latter strain rate limit (due to inertia) as a function of the specific strength for a value of error r of 3% (variations smaller than 3% are typically not observable in Kolsky bar experiments). Three typical specimen sizes are chosen and three commonly used materials are also shown in the figure [33.16]. This is a useful approach to estimating the limiting strain rate in very-high-strain-rate experi-

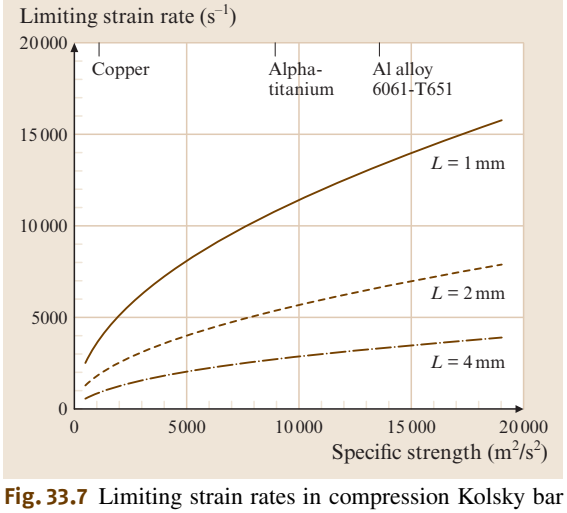

Fig. 33.7 Limiting strain rates in compression Kolsky bar experiments due to inertial errors in flow stress measurement

ments for a given specimen size and a known specific strength of the material. This is also helpful for clarifying the sometimes dramatic reported changes of flow stresses in the range of strain rates of $\approx 1\times10^{3}$ – $\approx 5\times10^{4}\,s^{-1}$, by helping to distinguish valid from invalid tests.

33.1.2 Extensions and Modifications of Kolsky Bars

A very large number of extensions and modifications of the traditional Kolsky bar system have been developed over the last five decades. Most of these are listed in Table I of the review by *Field* et al. [33.1], who include an exhaustive literature set. We discuss some of the key modifications in the rest of this section, focusing on some particular challenges.

Modifications for Ceramics

There are three major difficulties associated with testing ceramics in the conventional compression Kolsky bar. First, these materials are extremely hard, and thus are likely to cause damage to the bar ends. Second, these materials do not develop substantial plastic strain, so that failure will be caused essentially in the elastic domain and specimen strain can be very difficult to measure. Third, since these materials are extremely brittle, the specimen design can easily introduce defects that will cause premature failure, raising the question of whether the material properties can be measured. An excellent summary of these issues is presented in the ASM Handbook article by *Subhash* and *Ravichandran* [33.26]. The first of these difficulties can be somewhat mitigated by using special inserts (called platens) at the end of the bars that are made of even harder ceramics, e.g. [33.27]. The second and third difficulties are much harder to address. The fact that failure occurs immediately after the elastic domain means that it becomes very important to ensure a stress equilibration was in the specimen, and this cannot be done with the traditional trapezoidal pulse. The best way to resolve this issue is to use a controlled rise time for the incident pulse, and to ensure that equilibration occurs well before failure develops. The incident pulse shape is controlled [33.23] by using a buffer material or a pulse-shaper material at the projectile/impact-bar interface (this material is typically a soft metal, for example copper) [33.28]. The question of when equilibration occurs remains a matter of some debate. A rule of thumb that is commonly used is that at least five reverberations of the elastic wave should occur before the difference in the stress in the two sides of the specimen becomes sufficiently small to be ignored. This also generates limits on the effective strain rates that can be developed for valid Kolsky bar testing [33.29]. Note that for the harder hot-pressed ceramics, the specimen strain is extraordinarily difficult to measure because of indentation of the ceramics into the platens.

The specimen design also has significant impact on the results obtained in Kolsky bar experiments on ceramics. In a sense, it is possible to view experiments in ceramics in one of two modes. One wishes to measure the properties of the ceramic itself – this is often the original intent. However, one may instead be examining the properties of the ceramic specimen as a structure, since the stress concentrations at the corners and the edges can have such a strong influence on the failure process. In the quasi static mechanical testing of ceramics, researchers have gone to great lengths to optimize the specimen design. This degree of optimization has not yet been accomplished in the dynamic testing of ceramics. Several specimen designs have been proposed and used, e.g. [33.30]. It appears that substantial gains in understanding can be obtained by juxtaposing high-speed photography (Fig. 33.8) of specimen deformation during loading with the recorded stress-time curves [33.27]. The figure demonstrates that, in this polycrystalline ceramic:

1. axial splitting is *not* the mode of compressive failure and
2. that the interaction of flaws is of great importance in dynamic brittle failure under compression.

Modifications for Soft Materials

The testing of very soft materials (such as polymers and soft tissues) in the Kolsky bar represents the alternate extreme of difficulty in comparison to testing ceramics [33.31]. The two primary difficulties here are

1. the transmitted stress is very small, and so can be measured only with great difficulty, and
2. equilibration of the stress in the specimen can take a very long time [33.32].

There have been substantial improvements in the testing of soft materials over the last two decades, primarily involving the use of polymer or magnesium bars with small elastic moduli, so that small stresses can still generate large enough strains to measure [33.33]. The use of semiconductor strain gages instead of foil gages has also provided significant improvement [33.33]. The equilibration question is addressed sometimes by the

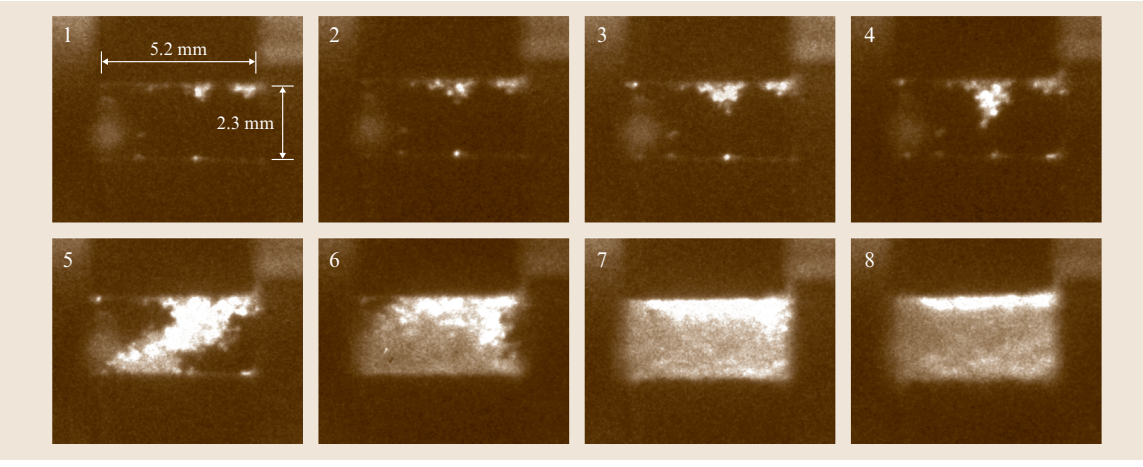

Fig. 33.8 High speed photographs of the development of microcracks in a transparent polycrystalline ceramic (AION) under dynamic compression along the horizontal axis [33.27]. The interframe times is 1 μs and each exposure times is 20 ns

direct measurement of force using piezoelectric quartz gages [33.34]. All of these approaches require great care with both experimental setup and data analysis [33.35]. One particularly important question that must be explicitly addressed for each material is that of material incompressibility.

Modifications for High Temperature Testing

The most common approach to running high temperature Kolsky bar experiments is to simply heat the specimen while it is in contact with the input and output bars (typically inside a tube furnace), allowing a strong temperature gradient to develop within the bars. If an estimate of the temperature gradient can be made, its effect can be compensated for by making the proper adjustments to the wave-speeds due to the temperature-dependent elastic modulus of the bar material [33.36]. Such techniques have limitations on the attainable specimen temperature that are imposed by heat conduction in the bars and by the properties of the bar materials. One solution to this problem has been to provide an insulating layer between the specimen and bars in the form of a short length of impedance-matched ceramic bar [33.37]. A variant of this technique has been used to perform high temperature torsion tests [33.38]. One method of providing rapid heating in such an arrangement (for conductive specimens) is induction heating [33.37].

A second, more modern approach to running high temperature experiments in the Kolsky bar is to heat the specimen alone, and then to bring the bars into contact with the specimen just before impact [33.39]. This setup has the advantage of reducing temperature gradients in the bars, and the added benefit of requiring relatively small energy inputs to heat the specimen. The major design issue in such a system is the *cold contact time* – the duration of time over which the input and output bars are in contact with the specimen before the arrival of the incident wave. During this contact time, thermal gradients develop within the specimen, and the overall specimen temperature drops by an amount that is typically not recorded. Various arrangements have been used to reduce this cold contact time, e.g. [33.39] and [33.40]. Approaches to heating the specimen include RF heating and radiative heating [33.39]. Conductive heating and pulse heating approaches have also been used to develop very large heating rates in metallic specimens [33.41].

Tension Kolsky Bars

A version of the Kolsky bar system that is effective in tension was developed in the 1960s [33.42]. The basic principle of this system is identical to the compression system, except that a method for generating a tensile wave must be used, and special tension grips are required for the specimen. That are two basic approaches to generate a tensile wave in input bar. The first approach, known as an impact-tension approach, consists of firing a tubular projectile at a flange at the end of a bar, thereby generating a tensile wave within the bar. A variant of this approach uses a reaction mass and causes the reflection of a compressive wave as a tensile

wave [33.43]. The second, and less common, approach consists of storing a large tensile strain within a section of a bar and then suddenly releasing it is so as to generate a tensile wave (this is known as the direct-tension approach) [33.44].

The gripping of tensile specimens requires some care, because otherwise the spurious wave reflections from the grips would make it difficult to interpret the experiments. Commonly used grips include threaded ends and adhesively bonded ends. A general rule of thumb is that if the gripped ends are made of the same material as the bar and are no longer than the bar diameter, then the effect on the wave propagation will be minimal. An example of the direct-tension Kolsky bar is shown in Fig. 33.9 [33.45]. A tensile force is applied to a section of the input bar using the hydraulic actuator system, while the rest of the input bar is restrained using a friction clamp. When the friction clamp is suddenly released, a tensile pulse propagates down the input bar and loads the specimen in tension; part of this incident pulse is transmitted into the output bar, and part is reflected back to the input bar. Strain gages are mounted on the input and output bars to measure elastic strain in the bars. Using these strain gages, the incident, reflected and transmitted pulses in the bars can be measured. As before, the transmitted pulse provides the stress history of the specimen, while the reflected pulse provides the strain rate history (which can then be integrated over time to obtain the specimen strain). Multiple strain gauge stations may be needed in order to separate out the incident and reflected pulses. The equations are identical to those used for the compression Kolsky bar, but the specimen length replaced by a gauge length on the tensile specimen. A full tensile stress-strain curve is obtained at fairly high strain rates (on the order of 10^2–10^3 s^{-1} using this system).

However, the traditional approach to obtaining the specimen strain in the tension Kolsky bar provides an inaccurate measure of strain, in general. This is because it measures the relative displacement of the two specimen-bar interfaces, and converting this to specimen strain requires an assumption of a specimen gauge length (this is very well known in compression, but is not well defined in tension). Since fillets are required in tensile specimens in order to avoid failure due to stress concentrations at the specimen flanges, the non-uniform deformation developed at the flanges contributes to the total deformation of the specimen. It is therefore difficult and at times impossible to determine the effective gauge length to be used in the calculation of specimen axial strains [33.42]. Ideally one should have a strain-gage mounted directly on the specimen to provide measures of strain throughout the experiment. One alternative approach is to use a high-speed camera to directly measure the specimen diameter and length during an experiment. A second alternative is to use the Laser Occlusive Radius Detector (LORD) technique to directly determine the local specimen strains during high-strain-rate experiments [33.45]. This approach requires the assumption of incompressibility in the specimen in order to estimate the axial specimen strain (an assumption that

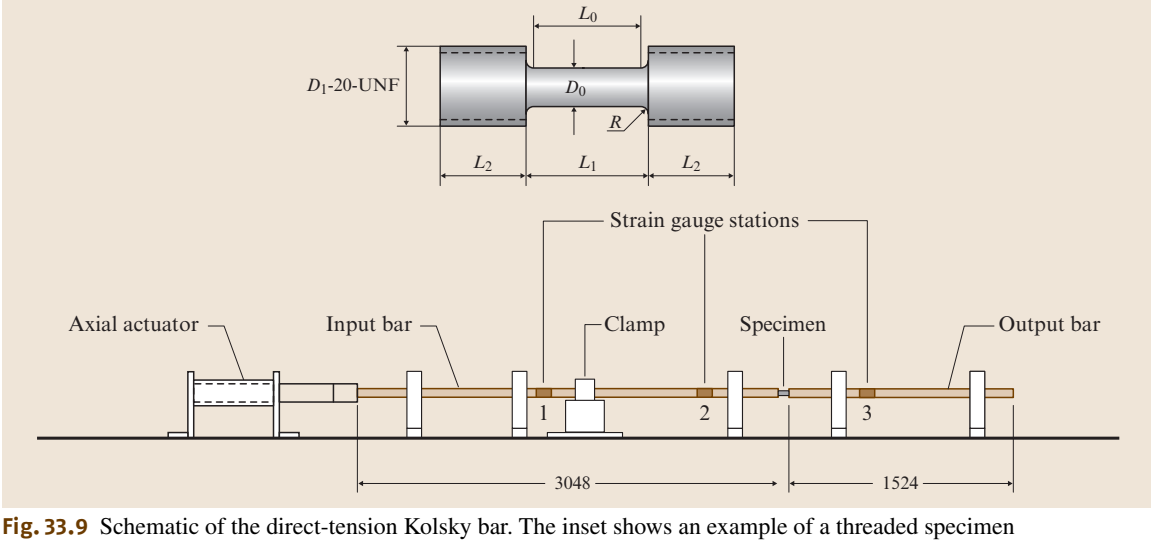

Fig. 33.9 Schematic of the direct-tension Kolsky bar. The inset shows an example of a threaded specimen

is typically not valid once necking begins). However, it is capable of measuring fairly large plastic strains, which are generally not measurable using standard on-specimen strain gauges because they debond during the deformation.

Torsional Kolsky Bars

The torsional Kolsky bar is an adaptation of the compression Kolsky bar that is used to generate high strain rate shearing deformations within typically tubular specimens [33.46]. An excellent summary of the technique is presented by *Hartley* et al. [33.47]. A schematic of such a device is presented in Fig. 33.10. The principle of operation of this bar is identical to that in the tension Kolsky bar, except that a torsional wave is now propagated down the input bar towards the specimen. One advantage of the torsional Kolsky bar is that primary-mode torsional waves are not dispersive in the bar, so that dispersion corrections are not necessary. A second advantage of this system is that (in principle) very large shearing strains can be sustained and so material behavior can be studied over very large strain regimes. That is, the difficulties associated with maintaining friction during large deformations (in the compression bar) and avoiding necking (in the tension bar) are avoided in the torsional bar system. Further, radial expansion and contraction are not significant in torsion of isotropic materials, so that the inertial and end effects present in the tension and compression tests are absent in the torsional Kolsky bar experiment. However, shear bands may develop during torsional deformations: in fact this is one of the most common applications of the torsional bar system [33.48].

A significant experimental concern in the setup of the torsional Kolsky bar system is the avoidance of bending waves. Flexural waves in a long bar may have signal content propagating at speeds similar to that of the torsional wave, resulting in some difficulties in wave analysis. It is particularly important that the friction clamp design not generate flexural waves within the laws – note in particular that the use of heavy friction clamps is *not* an advantage. Careful placement of the supports and specific initial measurement of the propagation of bending waves within the bar is warranted.

The difficulties associated with specimen gripping are also an issue with the torsional Kolsky bar design. Typical approaches to gripping the specimen include the use of adhesives, asymmetric flanges, and various types of compression grips. Specimen design is critical, with the usual questions associated with the definition of specimen gauge length and definition of fillet radii. It is recommended that a full finite deformation analysis of the plastic deformation of a specimen be performed before using the given specimen design with an experiment.

The equations associated with the use of the torsional Kolsky bar system are different in detail, but not in character, from those used for the compression Kolsky bar system. A full description of the relevant equations is presented by *Hartley* et al. [33.47]. The primary distinctions arise because of the torsional mode: one must consider torques and angular velocities rather than axial forces and translational velocities. We note that a response diagram very similar to Fig. 33.6 may also be constructed for the torsional Kolsky bar, and may be used in a very similar way to accomplish experimental design. Examples of show stress versus shear-strain curves obtained using the torsional Kolsky bar are presented in Fig. 33.15 for the aluminum alloy 6061-T6.

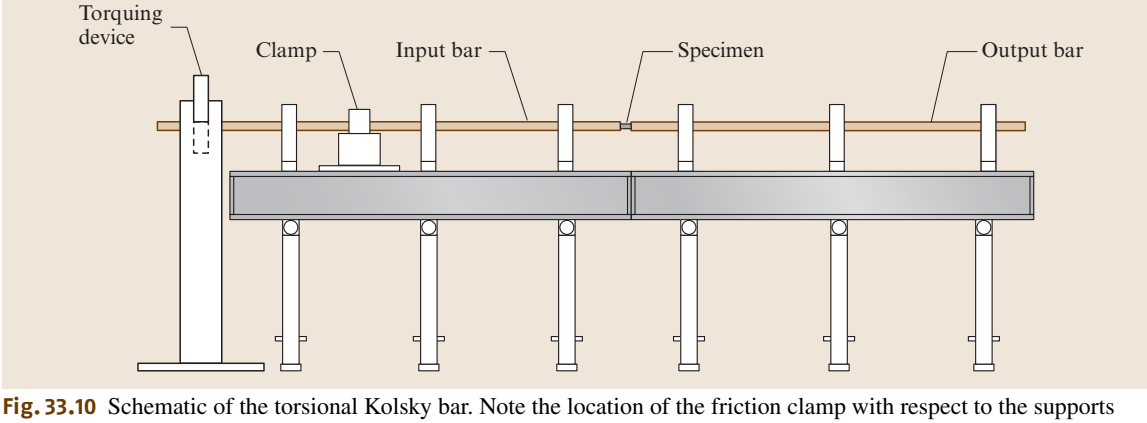

Fig. 33.10 Schematic of the torsional Kolsky bar. Note the location of the friction clamp with respect to the supports

The torsional Kolsky bar system has also been modified to perform high-temperature testing at high shear strain rates [33.38]. In this approach the necessity of using grips on the specimen can be turned into an advantage, with the grips acting as thermal insulators and reducing the heating of the bars themselves.

33.1.3 The Miniaturized Kolsky Bar

Attempts to push the Kolsky bar arrangement to higher strain rates have led to three modifications: decrease of the specimen length, direct impact on the specimen (thus increasing effective velocity), and miniaturization of the entire system. The first approach, with smaller specimen sizes, is typically limited by frictional effects. The second approach is the so-called direct impact technique, a projectile directly impacts a specimen placed in front of an elastic bar (which operates like the output bar in the regular version of the Kolsky bar). Since there is no input bar, the impact velocity can be very high. However, because of the absence of an input bar, there is no reflected signal from which the strain rate and strain in the specimen can be extracted. Strain measurement in the direct impact approach has been addressed in several ways, including

1. assuming the projectile is effectively rigid [33.49] and
2. measuring the velocity of the back surface of the projectile [33.50].

Gorham [33.51] obtained strain rates of $4\times10^4\,\mathrm{s}^{-1}$ in direct impact using a high-speed camera for strain measurement, and even higher rates were obtained in a similar configuration by *Safford* [33.52]. *Gorham* et al. [33.53] and *Shioiri* et al. [33.54] obtained the strain in direct impact experiments by *assuming* that stress equilibrium is satisfied throughout the deformation; strain rates of $2–4\times10^4\,\mathrm{s}^{-1}$ are claimed. *Kamler* et al. [33.55] developed a very small (1.5 mm dia.) direct impact Kolsky bar and performed experiments on copper at very high strain rates of 6×10^3 to $4\times10^5\,\mathrm{s}^{-1}$; again, stress equilibrium was assumed.

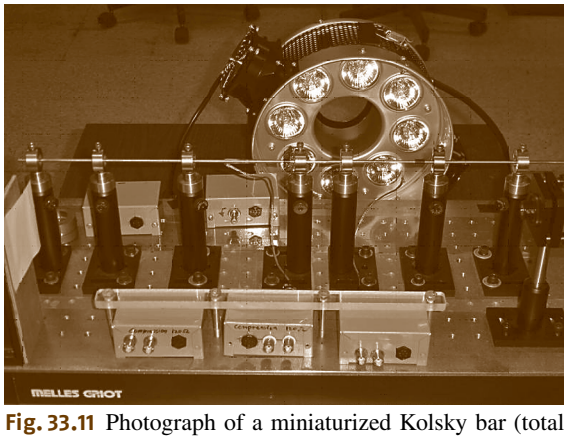

Fig. 33.11 Photograph of a miniaturized Kolsky bar (total length of 30″)

In the third approach, several fully miniaturized versions of the compression Kolsky bar have been developed (e.g., see *Jia* and *Ramesh* [33.16]). In the Jia and Ramesh version (see Fig. 33.11), the bars are on the order of 3 mm in diameter and 30 mm long, and may be made of maraging steel or tungsten carbide. Sample sizes are cubes or cylinders on the order of 1 mm on a side; cube specimens are used when the failure mode must be imaged using a high-speed camera, or when the amount of material is so small that only cuboidal specimens can be cut.

Very high strain rates (up to $5\times10^4\,\mathrm{s}^{-1}$) can be attained in miniaturized systems, while retaining the ability to study materials at strain rates as low as $1.0\times10^3\,\mathrm{s}^{-1}$ (the maximum achievable strain-rate is limited by an inertial correction and varies with the material being tested). Both computational and experimental results have shown that this extended capability can be attained without violating the requirements for valid high-rate testing, and indeed while improving the quality of the experimental results in terms of precision and accuracy [33.16]. The technique is simple, and the entire system can be designed to fit on a desktop – the technique is therefore sometimes referred to as the *desktop Kolsky bar*.

Equilibration of stresses can be rigorously checked from both sides of the specimen in the experiment even during the highest rate deformations that can be attained. Both experiments and simulations show that rapid equilibration of the stress can be achieved even at very high strain rates. However, effective lubrication remains critical. The miniaturized system makes it possible to reach a very high strain rate in a small sample with a relatively high l/d ratio, thus minimizing the influence of friction. Inertial errors in stress measurement are significantly reduced with the smaller specimens.

A comparison of the response measured by this miniaturized technique with the results of the traditional compression Kolsky bar system is presented in Fig. 33.12 for 6061-T6 aluminum alloy. This figure shows the rate-sensitivity over an extended range of strain rates that is not attainable with the traditional technique. Even higher-strain-rates can be attained

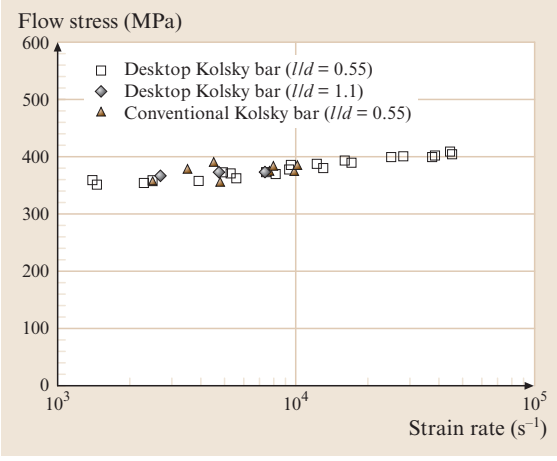

Fig. 33.12 Comparison of results obtained using the miniaturized and traditional compression Kolsky bars. The material is 6061-T6 aluminium alloy

using the pressure-shear plate impact experiment, described et seq.

The miniaturized Kolsky bar or *desktop Kolsky bar* experimental technique is particularly effective when it comes to understanding the properties of nanostructured materials, or of materials with very fine grain sizes. Note, however, that the small specimen sizes can make it difficult to use this approach with materials (such as solders) that have large grain sizes or a large microstructural length scale.

33.1.4 High Strain Rate Pressure-Shear Plate Impact

The high strain rate pressure-shear (HSRPS) plate impact technique was developed to study the shearing behavior of materials undergoing homogeneous shearing deformations at extremely high shear rates $10^4 - 10^6\,\mathrm{s}^{-1}$, while under superimposed hydrostatic pressures of several GPa. A detailed description of this technique is provided by *Klopp* and *Clifton* [33.56].

The experiment involves the impact of plates that are flat and parallel but inclined relative to their direction of approach (Fig. 33.13). The specimen consists of a very thin (of the order of 100 μm thick), very flat plate of the material under investigation. This thin specimen is bonded to a hard plate (the *flyer*), itself carried on a projectile which is launched down the barrel of a gas gun towards a stationary target or *anvil* plate. The projectile velocity ($\boldsymbol{V}_0$) at impact may be decomposed into a normal component $u_0 = \boldsymbol{V}_0 \cos\theta$ and a transverse

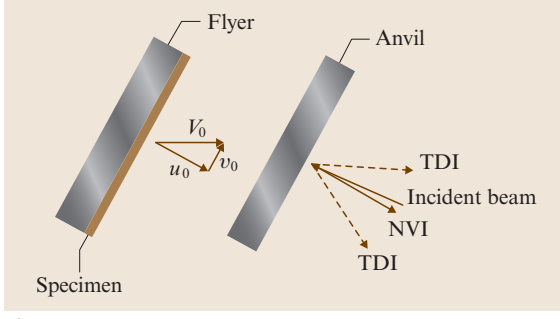

Fig. 33.13 Schematic of the high-strain-rate pressure-shear plate impact experiment. The specimen thickness is graetly exaggerated for clarity

component $v_0 = \boldsymbol{V}_0 \sin\theta$, where θ is the angle between the normal to the plates and the direction of flight of the projectile.

The target is positioned in a special fixture (known as the target-holder) within an evacuated chamber. The flyer and the anvil plates are aligned before impact using an optical technique developed by. Rotation of the projectile is prevented by a Teflon key in the projectile, which glides within a matching keyway machined in the barrel. The misalignment (*tilt*) between the two impacting plates is obtained by measuring the times at which the flyer makes contact with four pins that are mounted flush with the impact face of the target. Tilts better than 1 milliRadian are routinely achieved in these experiments.

At impact, plane longitudinal (compressive) and transverse (shear) waves are generated in the specimen and the target plate (Fig. 33.14) propagating at the lon-

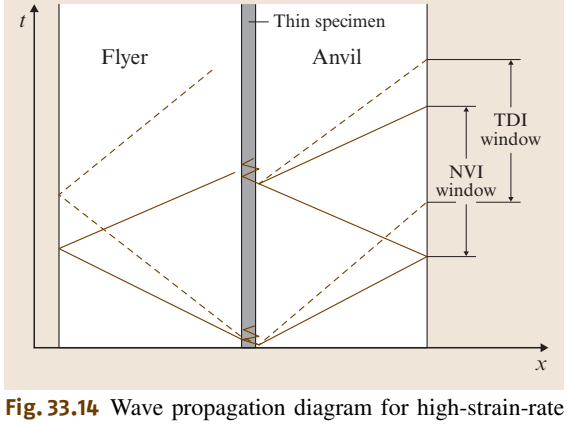

Fig. 33.14 Wave propagation diagram for high-strain-rate pressure-shear plate impact, with the specimen carried on the flyer

gitudinal wave speed c_l and the shear wave speed c_s. These waves reverberate within the specimen, resulting in a buildup of the normal stress and of the shear stress within the specimen material. Information on the stress levels sustained by the specimen material is carried by the normal and transverse waves propagating into the target plate. Since the target remains elastic, there is a linear relationship between the stresses and the particle velocities in the target plate. Thus it is sufficient to measure the normal and transverse particle velocities in the target plate to deduce the stress state and deformation state within the specimen. The entire experiment is completed before any unloading waves from the periphery of the plates arrives at the point of observation, so that only plane waves are involved and a one dimensional analysis is both sufficient and rigorously correct. Like most plate impact experiments, this is a uniaxial strain experiment in that no transverse normal strains can occur during the time of interest.

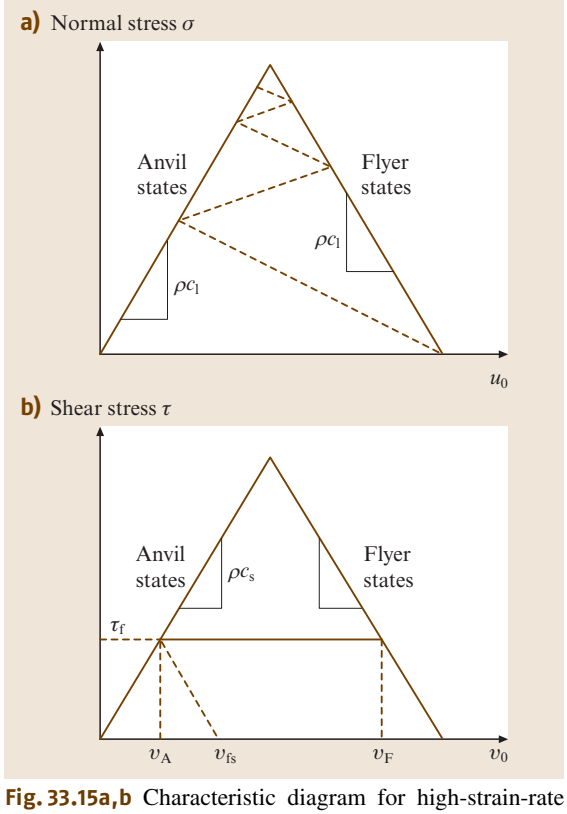

Fig. 33.15a,b Characteristic diagram for high-strain-rate pressure-shear plate impact. **(a)** Development of normal stress and **(b)** shear stresses in the specimen

Measurements of the particle velocities at the free surface of the target plate are made using laser interferometry off a diffraction grating that is photodeposited onto the rear surface. The normal velocity and the transverse displacement at the center of the rear surface of the target are measured using a normal velocity interferometer (NVI) and a transverse displacement interferometer (TDI), e.g. [33.57]. The laser used is typically either an ion laser or a diode-pumped, frequency doubled, Nd:YAG laser. The interferometric signals are captured by high speed silicon photodiodes (with rise times < 1 ns) and recorded on high-speed digitizing oscilloscopes, using typical sampling rates of 1 ns/point and bandwidths of 500 MHz – 1 GHz.

The longitudinal and transverse waves generated on impact (Fig. 33.14) reverberate within the specimen, remaining loading waves since the impedance of the material of the flyer and target plates is (by design) higher than that of the specimen materials. The development of the stress in the specimen is most easily seen in the characteristics diagram of Fig. 33.15. The characteristic relations ($\sigma \pm \rho c_l u = \text{const.}$ or $\tau \pm \rho c_s v = \text{const.}$, with σ and τ the normal stress and shear stress and u and v the normal and transverse particle velocities respectively; ρ is the density of the plate material) in the linear elastic plates give us

$$\begin{aligned} -\sigma + \rho c_l u &= \rho c_l u_0 \,, \\ \tau + \rho c_s v &= \rho c_s v_0 \,, \end{aligned} \tag{33.23}$$

in the flyer and

$$\begin{aligned} -\sigma + \rho c_l u &= 0 \,, \\ \tau + \rho c_s v &= 0 \,, \end{aligned} \tag{33.24}$$

in the anvil. Thus all states in the flyer will lie on the solid line passing through u_0 (for the normal stress, Fig. 33.15a) or v_0 (for the shear stress, Fig. 33.15b), while all states on the anvil will lie on the solid line passing through the origin. In the case of the normal stress (Fig. 33.15a), the normal stress in the specimen must always lie along the characteristic lines shown by the dashed lines. The state of the specimen at any given time is given by the intersection of the characteristic line of specimen with either the characteristic line of the anvil or the characteristic line of the flyer. If there is a difference in the normal velocities on the two sides of the specimen (the flyer side and the anvil side), then the specimen will continue to be compressed in the normal direction. However, the plate impact experiment is a uniaxial strain experiment rather than a uniaxial stress experiment like the Kolsky bar. The continued

compression along the normal direction thus implies a change in volume. Due to the finite compressibility of the specimen, the normal stress in the specimen attains an equilibrium value (corresponding to the intersection of the flyer and anvil characteristics) given by

$$\sigma_{\mathrm{eqm}} \cong \frac{1}{2}\rho c_{\mathrm{l}} V_0 \cos\theta \,, \tag{33.25}$$

where ρc_{l} is the acoustic impedance of the steel, V_0 is the projectile velocity and θ is the skew angle. At equilibrium, the hydrostatic pressure in the specimen can be approximated to the normal compressive stress, differing from it by at most the strength of the specimen material. Note that the difference in normal velocities on the two sides of the specimen continuously decreases. Thus the normal strain-rate in the high-strain-rate pressure-shear plate impact experiment is initially high but tends towards zero, actually approximating zero when normal stress equilibrium has been achieved. This is again a result of the uniaxial strain condition.

The shear stress in the specimen also increases with each reverberation of the shear wave within the specimen (Fig. 33.15b), until the specimen starts flowing at a stress level τ_{f} (the flow stress). Thereafter, a finite difference in the transverse velocity can be maintained across the two surfaces of the specimen (unlike the normal velocity situation, it is possible to sustain a difference in transverse velocities across the specimen because the uniaxial strain condition does not present a constraint in this case). The velocity difference $v_{\mathrm{F}} - v_{\mathrm{A}}$ also corresponds to (see Fig. 33.15b) the velocity difference $v_0 - v_{fs}$, where v_{fs} is the transverse free-surface velocity measured at the rear surface of the target using the TDI. The nominal shear strain rate in the specimen is then given as

$$\dot{\gamma} = \frac{V_0 \sin\theta - v_{fs}}{h} \,, \tag{33.26}$$

where h is the specimen thickness. The nominal strain rate in the specimen can be integrated to give the nominal strain history in the specimen:

$$\gamma(t) = \int_0^t \dot{\gamma}(\tau)\,\mathrm{d}\tau \,. \tag{33.27}$$

The shear stress history in the specimen is obtained from the transverse particle velocity history using the elastic characteristics of the target plate (Fig. 33.14b)

$$\tau(t) = \rho c_{\mathrm{s}} v_{\mathrm{A}} = \frac{1}{2}\rho c_{\mathrm{s}} v_{fs}(t) \,, \tag{33.28}$$

where ρc_{s} is the shear impedance of the anvil plate. The shear stress and the shear strain in the specimen can now be cross-correlated to give the shear stress-shear strain curve (Fig. 33.16) for the material tested at an essentially constant shear rate corresponding to (33.26).

Examination of (33.25)–(33.28) shows that the critical measurements that must be made during the experiment are of the projectile impact velocity V_0 and the transverse free-surface particle velocity v_{fs}. The latter particle velocity is measured using the transverse-displacement-interferometer [33.57]. The projectile impact velocity can be measured in a number of different ways. These include measuring the times when the projectile comes in contact with specific pins placed a known distance apart; measuring the times when the projectile crosses two magnetic or radiofrequency sensors or laser beams that are spaced a known distance apart; or using a Laser Line Velocity Sensor [33.58]. Finally, the misalignment (*tilt*) between the flyer plate-specimen combination and the anvil plate must be measured for every test, both for purposes of diagnostics and to remove small components of the normal velocity that may show up within the transverse velocity signal due to the misalignment.

The high strain rate pressure-shear plate impact technique is capable of achieving shear rates of 8×10^4 to $10^6\,\mathrm{s}^{-1}$, depending on the specimen thickness, [33.57–59]. A version of this experiment that is designed to allow recovery of the specimen (for mi-

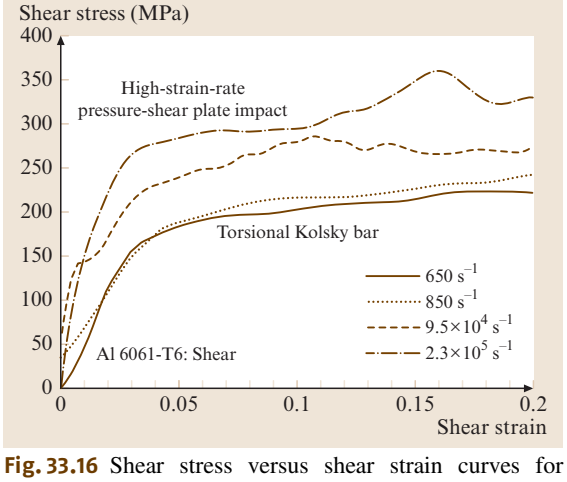

Fig. 33.16 Shear stress versus shear strain curves for 6061-T6 aluminium alloy obtained using high-strain-rate pressure-shear plate impact, compared with those obtained usinf the torsional Kolsky bar

crostructural examination) after a single high-strain-rate shear loading has also been developed [33.60]. The primary (33.25)–(33.28) can be rewritten to provide a locus of test response, as presented for the Kolsky bar in Fig. 33.6. Here we find that the test requires that the shear stress and the shear strain rate obey the relationship $\tau = 0.5\rho c_s\,(V_0 \sin\theta - \dot{\gamma} h)$, representing the test response line. The maximum shear strain rate that can be attained is $\dot{\gamma}_{max} = V_0 \sin\theta / h$ (and corresponds to $\tau = 0$), while the maximum shear stress that can be attained is $\tau_{max} = 0.5\rho c_s V_0 \sin\theta$ (and corresponds to the apex of the characteristic triangle in Fig. 33.15). The specific shear stress and shear rate obtained in a given test is the intersection of the material response curve with the test response line, as in Fig. 33.6.

The superimposed hydrostatic pressures that can be exerted during the high-strain-rate pressure-shear plate impact experiment may be as high as 10 GPa, depending on the impedances of the flyer and target plates and the projectile velocity. The superimposed hydrostatic pressures must always be remembered when comparing high-strain-rate pressure-shear plate impact data with data obtained using the other techniques shown in Fig. 33.1, since all of the other techniques can generate essentially uniaxial stress states, typically corresponding to low hydrostatic pressures. In particular, while the effect of pressure on the flow stress of most metals is negligible in comparison with the effect of strain-rate, the effect of pressure on the strength of polymers and amorphous materials may be substantial (even in comparison with the effect of strain-rate).

33.2 Wave Propagation Experiments

Experiments designed to study the propagation of large amplitude stress waves within materials constitute a very broad class of *impact* experiments. Note that we do not include in this category those experiments that are designed to study the propagation of waves within structures - such experiments are better considered in discussions of structural dynamics or of elastic wave guides (see photoacoustic characterization chapter). Our interest here is in experiments that examine the interactions of waves with materials, particularly exciting inelastic modes such as plasticity, cracking or other kinds of damage. In contrast to the previous section, the experiments in this section all generate strain rates and stress states that vary in both space and time, and the wave propagation is fundamentally dispersive because of material behavior.

In broad terms, wave-propagation experiments of this type fall into the same two categories considered in the previous section: bar wave experiments [33.61–66] and plate impact experiments, or more specifically, uniaxial-stress wave propagation experiments and uniaxial-strain wave propagation experiments. The plate impact experiments are far more commonly used, since they can explore a wider range of the phenomena that arise in impact events, and so we focus on such experiments here. It is perhaps worth pointing out a fundamental feature of large amplitude wave propagation in materials: in the timescales associated with the wave propagation, it is typically not possible to observe the far-field stress state, and so locally one is typically exploring the uniaxial strain condition. In other words, some local confinement is an inherent characteristic of large amplitude wave propagation in materials as a result of impact. This can make it difficult to compare results obtained at ultra-high strain rates (typically obtained with uniaxial-strain experiments) with results obtained at high and very high strain rates (typically obtained with uniaxial stress experiments), particularly if the material has pressure dependent properties.

The strain rates developed in large-amplitude wave propagation experiments (where shocks are developed) can be of the order of 10^6–$10^8\ s^{-1}$, but exist only for a short time behind a propagating wave front, and because of inelastic dissipation (as well as reflections from surfaces), the strain rates will vary with position within an impacted plate. Note also that the temperatures behind the wave front may be substantial, and must be accounted for as well. Comparisons of material properties estimated using wave propagation experiments and high-strain-rate experiments (the distinction made in this chapter) can therefore require careful parsing of experimental conditions.

33.2.1 Plate Impact Experiments

The basic concept of the plate-impact experiment has been touched on in the description of the high-strain-rate pressure-shear plate impact experiment above. A flyer plate is launched down a gun barrel towards a stationary target plate, typically using a gas gun for launch. The flyer plate is normally carried on a projectile known as a sabot, and is launched at velocities

ranging from a few tens of meters per second up to several kilometers per second using a variety of gas and powder guns. The flyer plate may impact the target plate at normal incidence, resulting in what is called a normal plate impact experiment. In oblique plate impact experiment consists of an impact that occurs at an angle as described in the pressure-shear plate impact experiment. The vast majority of plate impact experiments that are performed today are normal plate impact experiments, largely because oblique plate impact experiments typically require a keyed gun barrel to prevent rotation of the projectile during flight. We consider only normal plate impact experiments in the remainder of this section.

A schematic of the simplest form of the normal plate impact experiment is shown in Fig. 33.17. The minimum diagnostics that are typically obtained consist of measurements of the projectile impact velocity and the rear surface particle velocity. Once the impact occurs, normal uniaxial-strain compressive waves will be propagated in both the flyer and the target. The case where these waves are elastic is not interesting. Typically the target plate is expected to deform inelastically during the experiment, and in most experiments both flyer and target will do so. If the impact velocity is sufficiently high, one or both of the propagating waves within the plates will be inelastic. At velocities just above the velocity required to cause yield of the target material, both elastic and plastic waves will propagate into the target, with the elastic *precursor* propagating at a higher wave speed. Significantly higher impact velocities will result in the propagation of shock waves into the plates. The propagation of plastic waves within materials is a topic of some interest; however, the majority of plate impact experiments are conducted at velocity sufficiently high to generate shock waves within the plates, and so we will describe shock wave experiments in some detail.

It should be noted that the strain state in normal plate impact experiments is the uniaxial strain state only for a finite time. Once release waves from the boundary of the plates arrive at the point of interest, the strain state is no longer uniaxial-strain, and much more complex analyses are necessary. However, before the release waves arrive at the point of interest (for instance, the location at which particle surface velocities and displacements are being measured using interferometry), the strain state is rigorously one-dimensional and can be analyzed much more easily. Longer experimental times in the uniaxial-strain condition can be obtained by using larger diameter plates, but the increased cost of performing such experiments with large diameter plates is substantial. Typical experiments are performed with plate diameters on the order of 50 mm.

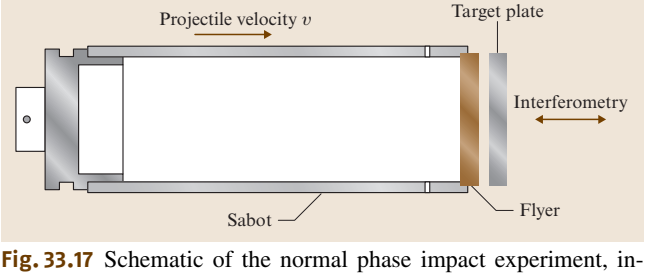

Fig. 33.17 Schematic of the normal phase impact experiment, including the sarbot

Shock Wave Experiments

In any uniaxial strain wave, there is always a difference between the normal stress σ_a (the stress along the direction of wave propagation) and the transverse stress σ_t (the stress transverse to the direction of wave propagation, which arises because of the uniaxial-strain constraint). The difference between these two stresses can be considered to be a shear stress and is of the order of magnitude of the deviatoric strength (yield strength for metals) of the material. The difference in the amplitude σ_a of the stress wave and the propagating pressure ($p = (\sigma_a + 2\sigma_t)/3$, all stresses defined as positive in compression) is $(2/3)(\sigma_a - \sigma_t)$. Since this latter quantity is of the order of magnitude of the flow stress, the difference between the longitudinal stress and the pressure is of the order of the strength of the material.

When the amplitude of the stress wave is extremely large in comparison to the strength of the material, the stress wave may be approximated as a shock wave, and treated essentially as a problem in hydrodynamics. A shock wave is a sharp discontinuity in pressure, temperature energy and density (more specifically, a shockwave is a traveling wave front across which a discontinuous adiabatic jump in state variables occurs). There are several excellent reviews of shock wave propagation ([33.67, 68]). The application of the balance of mass, balance of momentum and balance of energy conditions to the shock wave gives us the so-called Rankine–Hugoniot jump conditions across the shock [33.67]. These are:

$$\text{Mass}: \quad \rho_0 U_s = \rho_1 (U_s - u_p)\,, \tag{33.29}$$

$$\text{Momentum}: \quad P_1 - P_0 = \rho_0 U_s u_p\,, \tag{33.30}$$

$$\text{Energy}: \quad e_1 - e_0 = 1/2(P_1 + P_0) \times (v_0 - v_1)\,. \tag{33.31}$$

Here the initial state is denoted by the subscript 0 and the final state is denoted by the subscript 1; v represents the specific volume (the reciprocal of the density). In addition, an equation of state must be prescribed for each material that connects the specific internal energy of the material to the pressure, temperature and density. A shock wave generated during a plate-impact experiment propagates at a shock speed U_s that varies with the particle velocity u_p, and it is commonly observed that these two variables are related linearly or nearly so:

$$U_s = U_0 + s u_p \,, \tag{33.32}$$

where U_0 and s are material-specific parameters (the first is essentially the sound wave speed in the material). Large numbers of experiments have been performed to determine these parameters in various materials (e.g., a summary of such data is presented by *Meyers* [33.68] Table 4.1). Another useful reference is that by *Gray* [33.69].

The shock wave propagation literature is extensive, including a large number of conference proceedings from the biannual meetings of the American Physical Society Topical Group on Shock Compression of Condensed Matter published by the American Institute of Physics [33.70–74] and a series on the Shock Compression of Solids published by Springer [33.75–79]. Experimental details are often only presented in these conference proceedings, and so the reader is advised to examine these books carefully.

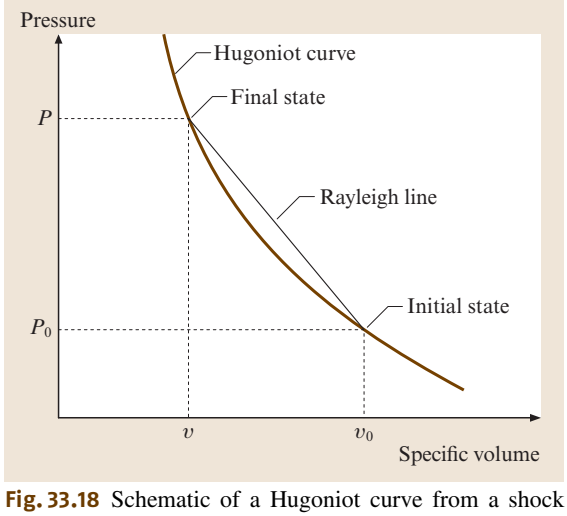

Fig. 33.18 Schematic of a Hugoniot curve from a shock experiment showing how the initial and final states are connencted by a Rayleigh line

The intent of most shock wave experiments is to measure a so-called Hugoniot curve for a material. A Hugoniot curve (Fig. 33.18) is the locus of all possible final states (e.g., in a pressure-specific volume space) attainable by a single shock from a given initial state. We note that such a curve couples the material response with the thermodynamics, and does not represent a true thermodynamic path. The shock speed U_s is given by the slope of the Rayleigh line shown in Fig. 33.18, and is thus clearly dependent on the particular final state.

Asig19]Should the figure be divided in “a” and “b”? Please check. an example, consider the shock wave analysis of the normal impact of two identical plates in the schematic experiment shown in Fig. 33.17. We assume that the impact velocity is $\boldsymbol{V}_0$ and that there is no unloading from the edges during the time of interest. In the moment of impact shock waves are generated in both the target and the flyer plates. What are the pressure and velocity states in the two plates after the shock? The initial conditions are that the target plate is initially at rest, while the flyer plate is initially moving at the impact velocity (Fig. 33.19). The interface condition is one of traction continuity and velocity continuity at the A-B interface between the two plates. Applying (33.30) and (33.32) on each side of the interface, we obtain

$$P_B = \rho_{0B} U_{0B} u_{pB} + \rho_{0B} s_B u_{pB}^2 \tag{33.33}$$

in the target and

$$P_A = -\rho_{0A}(U_{0A} + s_A u_{pA} + \boldsymbol{V}_0)(u_{pA} - \boldsymbol{V}_0) \tag{33.34}$$

in the flyer, with the subscripts A or B used to indicate variables in the target or flyer respectively. Thus the states at A and B (the pressure and velocity states immediately after the shock has been generated) are given by the solutions of (33.33) and (33.34). The solution is

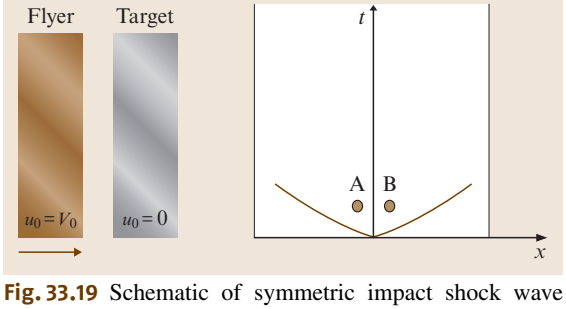

Fig. 33.19 Schematic of symmetric impact shock wave experiment. First phase of shock wave propagation in impacted plates

shown graphically in Fig. 33.20; note the similarity to the characteristics diagram in Fig. 33.15 for the high-strain-rate pressure-shear plate impact experiment. This approach is sometimes called the impedance matching method for determining the solution. Problems involving asymmetric impact can be solved in exactly the same way. We note that the release waves (reflections from the free surfaces) are somewhat more complicated, since release does not occur along the Rayleigh line but along the isentrope instead. Detailed approaches to the solution of specific shockwave problems are presented in the books by *Drumheller* [33.67], *Meyers* [33.68] and *Zukas* [33.80]

The major experimental issues associated with shockwave plate impact experiments are

1. the development of gun launching facilities at the appropriate velocities;
2. the accurate measurement of projectile velocity;
3. the measurement of the stress state within the specimen; and
4. the measurement of the particle velocities in the targets.

We do not discuss the first of these issues in any detail: such gun-launch facilities are typically extremely specialized facilities made by a small number of companies and national laboratories, and extraordinary precautions must be taken to ensure the safety of all laboratory personnel. Most of these facilities are either gas guns, light gas guns or powder guns, and for the higher velocities multistage guns are typically required. Since kinetic energy increases with the square of the velocity, reaching higher velocities typically requires the use of lower-mass sabots and flyers. Velocities greater than 10 km/s have been achieved with ≈ 1 g flyers using multi-stage guns at some national laboratories [33.81]. The second of these issues, the accurate measurement of projectile velocities, has already been dealt with in the section on high-strain-rate pressure-shear plate impact. The last two issues, the measurement of the stress state and the measurement of the particle velocity at these very short time scales are discussed in this section.

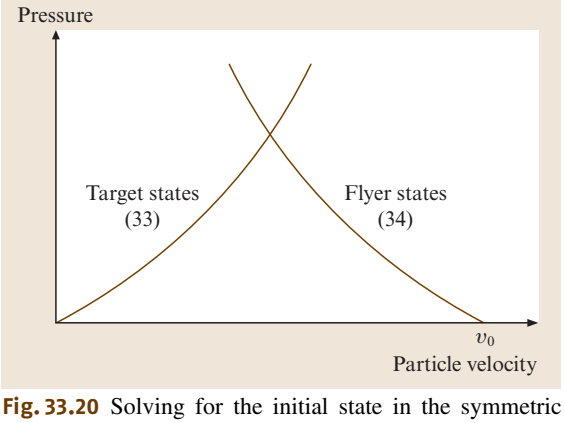

Fig. 33.20 Solving for the initial state in the symmetric impact shockwave experiment

There are several quantities that are of interest in a shock wave plate impact experiment. These are the normal stress, the transverse stress, the shock speed, the particle velocity in the direction of wave propagation (not all other particle velocity components are zero), the pressure and the temperature. Of the normal stress, the transverse stress and the pressure, only two of these have to be measured independently. Note that if the shock impedance of the material is known, then measurements of the particle velocity can be used to infer at least one of the stresses. Thus one needs in general to measure two stresses, the shock speed, one particle velocity and the temperature. All of these need to be measured with nanosecond resolution over time frames of several microseconds. The table below (adapted from [33.1]) lists some typical ways in which these quantities can be measured.

Excellent summaries of experimental techniques for the measurement of these quantities are provided in the recent review by *Field* et al. [33.1] and in a chapter by *Meyers* [33.68]. The installation of stress gauges within specimens (stress gauges must of necessity be placed within specimens rather than on free surfaces) is a difficult task to perform consistently, and individual laboratories have developed specialized ways of performing these installations. Some of the difficulties associated with the use of stress gauges are described by *Gupta* [33.82]. The use of *lateral* stress gauges to measure transverse stresses appears to be particularly difficult, and remains uncommon. However, excellent measurements of strength have been obtained using this technique [33.83].

The stress gauges that are used are either of the piezoresistive or piezoelectric types. Typical piezoresistive gages are manganin [33.84] or ytterbium [33.85] stress gauges. Manganin gauges are perhaps the most commonly used, being cheap and commercially available for use up to 40 GPa. Typical piezoelectric stress gauges include quartz [33.86] and PVDF [33.87], although PZT and lithium niobate gauges are also used. PVDF gages are typically used for stress levels up to 1 GPa, while quartz gages may be used up to

5 GPa. The particle velocity on the rear surface of the target is typically measured using laser interferometry. The rear surface may be a free surface, or may be interrogated through a transparent window material. The most common approach to performing such interferometry is using the velocity interferometer system for any reflector (VISAR) developed by *Barker* et al. [33.88–90]. Versions of the system that use fiber optic probes, and versions that can provide data from multiple points (the so-called *Line VISAR*) have been developed; the latter can be used to look at heterogeneous wave structures [33.91]. Most shockwave experiments are designed to provide a one-dimensional strain state, so that single-point measurements should be representative of the events. However, some of the phenomena that develop during shock wave propagation lead to heterogeneous structures. These include the development of *failure waves* and spallation. In such circumstances, it is a distinct advantage to be able to obtain full field information using high-speed photography (this is most useful for transparent materials) [33.92].

33.3 Taylor Impact Experiments

The most commonly used direct impact experiment is the Taylor impact experiment. The experiment involves the impact (at normal incidence) of a rod onto a plate (assumed to be nearly rigid). Substantial dynamic deformations are developed at the site of the impact, leading to a local expansion of the rod and the development of a final shape that depends on the impact velocity and on the properties of the material of the rod. An alternative version of the Taylor impact experiment involves a symmetric impact of two rods. The Taylor impact experiment has the advantage that it is extremely simple to perform. All that is needed is a facility for launching the rod at the desired velocity, and the ability to measure the deformed shape of the rod. However, the experiment has the disadvantage that it essentially represents an inverse problem: one must try to determine material properties on the basis of the macroscopic measure of an inhomogeneous deformation. Several improvements have been made to this experiment, including the use of high-speed photography to measure the process of deformation rather than simply the final deformation, and techniques for measuring the internal hardness variation within sections of the deformed bar. An excellent review of the Taylor impact experiment is provided by *Field* et al. [33.1].

33.4 Dynamic Failure Experiments

One must distinguish between the kinds of experiments needed to understand the deformation of a material and the kinds of experiments needed to understand a failure process within the material or structure. The former are most easily studied with experimental techniques that develop homogeneous stress fields, homogeneous strain fields and well-controlled loading. In such experiments, as in the high-strain-rate experiments described earlier in this chapter, as the deformation evolves, the stress fields and deformation fields remain nearly homogeneous, and a small number of measurements (typically single point or area averaged measurements) are sufficient to obtain information about the deformation and stress fields of interest. However, once a failure process begins in the material, the deformation field rapidly becomes localized, and the experimental techniques used to extract information using single-point or area-averaged measurements no longer provide adequate information. Understanding the failure process typically requires a different suite of experimental measurements, and often requires a completely different experimental design.

A simple example of this can be seen in the case of fracture: the uniaxial tension experiment is very well developed for the measurement of material behavior under uniaxial tension, but the utility of this experiment to determine the ability of the material to resist the propagation of cracks is minimal. Instead, specially designed fracture experiments are required. This is one reason why, although material scientists have a great affection for the simple tension experiment, they find it difficult to extract useful information about the toughness of a material by examining the elongation of the specimen in tension. A similar situation arises when understanding

the dynamic failure process: specialized experiments are required to measure the dynamic failure process, and normal high-strain rate experiments must be interpreted with care when failure processes are occurring.

The experimentalist in the dynamics of deformable solids does have one advantage over the experimentalist in the traditional mechanics domain. Most failure processes are inherently dynamic, and he/she may already have access to instruments with sufficient time resolution to resolve the failure process. However, there is also a potential complication. The failure process, itself dynamic, may be initiated by the arrival of a dynamic load. Thus, both slowly varying and rapidly varying loads may result in the development of dynamic failures.

There are three primary modes of failure in most engineering materials:

1. void nucleation, growth and coalescence,
2. crack nucleation, growth and coalescence, and
3. shear band development.

The first and third of these are typically associated with ductile failure, while the second is associated with brittle failure. However, all three modes may be observed simultaneously during a ductile failure event. Most experimental techniques in the dynamic failure literature are designed to examine the growth of a pre-existing void or crack, although the nucleation process may be of particular importance during dynamic failure [33.93]. The late stages of any failure process typically involve coalescence processes and can be the most difficult to resolve in an experiment. We begin by discussing experimental techniques associated with the measurement of void growth and shear band development under dynamic loading. We do not discuss experimental techniques for dynamic fracture in any detail, since this topic is heavily discussed in the literature [33.94]. It is important to remember that because these complex failure processes may feature interactions between the failure process, the dynamic loading, nearby free surfaces, and high strain rate material properties, a theoretical understanding of the failure process can be a great asset in designing appropriate experiments. Early experiments in this area were primarily concerned with defining the phenomenology of these failure processes, helping to determine which mechanisms should be included in the modeling. The development of improved analyses and much greater computational power now affords us the opportunity to perform experiments with the appropriate measurements to be able to extract parameters that characterize the failure process. Indeed, an early decision that must be made in experimental design is whether the objective is to determine the micromechanisms associated with the dynamic failure process or to provide characteristic parameters that define the sensitivity of the material to this particular failure process.

33.4.1 Void Growth and Spallation Experiments

At this time, analytical and computational papers on the dynamic growth of voids outnumber experimental papers by more than 10 to 1, attesting to the difficulty of performing controlled dynamic experiments on void growth. Most experiments that consider the dynamic growth of voids are plate impact experiments, although a few experiments have considered dynamic tension (for example using the tension Kolsky bar) with varying degrees of triaxiality [33.95] produced by inserting controlled notches. Dynamic tension experiments with controlled triaxiality are essentially dynamic versions of similar experiments that have been performed to examine the quasi-static process of void growth and coalescence [33.96]. Understanding these experiments requires a coupled computational and experimental approach (sometimes called a hybrid approach), since the stress state is deliberately nonuniform. The utility of the experiments is greatly improved if they are coupled with high-speed photography of the developing deformation, as well as the use of digital image correlation [33.97–103]. Comparison of computational and experimental results is particularly useful in examining such tension experiments [33.104]; we note, however, that such experiments alone are not sufficient for determining the mechanics associated with the failure processes that occur inside the specimen. Rather, such experiments help bracket the parameters and thus constrain the assumed failure model. Quantitative measurements of the internal deformations associated with the dynamic growth of voids would be ideal, but such measurements are not available in solids except with very expensive stereoscopic x-ray equipment. The first steps in this direction have been taken by the PCS group at the Cavendish [33.105].

Plate impact experiments that examine void growth are of two types. In the first type, pioneered by *Clifton* and his group at Brown [33.106–109], a pre-fatigued crack is generated within a target plate that is subjected to impact, such that a reflected tensile wave loads the crack. The existence of the prior crack generates a well-defined region within which the void growth can commence. This approach has been used with

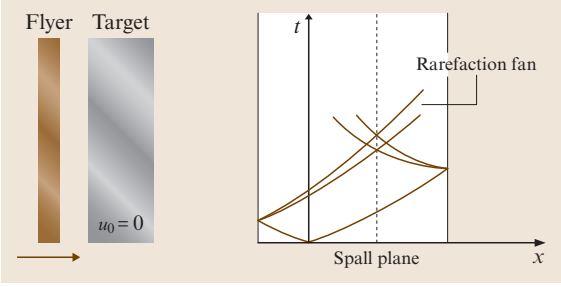

Fig. 33.21 Schematic and wave propagation diagrams for the spallation experiment. Note the location of the spall plane with respect to the two rarefaction fans

both brittle materials [33.106, 107] and ductile materials [33.108], and the loading has included both tensile and shear waves [33.109]. The technique has the advantage that the location of the prior crack is known, and the subsequent failure process can be studied using both the measured diffracted waves and the fracture surface morphology [33.110].

The second type of plate impact experiment of interest here is the spallation experiment [33.112, 113]. The basic approach is identical to that in the shock-wave experiments described in Fig. 33.19, with the difference that the phenomenology of interest is developed when the release waves interact (Fig. 33.21). The flyer is normally thinner than the target, and may be made of a different material. The wave propagation within this arrangement is shown in Fig. 33.21.

When the compressive shock waves reach the free surfaces of the flyer and the target plates, they are reflected as release waves. However, release waves unload along the isentrope rather than along the Rayleigh line (Fig. 33.18), so that a rarefaction fan is developed in each case. Very high tensile stresses are developed very rapidly at the location where the two rarefaction fans intersect, and the corresponding plane is called the spall plane. Voids nucleate, grow and coalesce along the spall plane, resulting in the separation of a piece of the target plate. This is called a spall failure or spallation (note the identical experiment can be performed for relatively brittle materials such as hardened steels). The development of the spall failure results in specific signatures in the particle velocity at the rear surface of the target plate which can be interpreted in terms of the *spall strength* of the material [33.114]. An excellent review of spallation experiments, and a discussion of the approaches to interpreting the results is presented by *Antoun* et al. [33.115].

The spall strengths of a large number of materials has been determined (Fig. 33.22), and a wide range of values is quoted for some cases. One of the key difficulties in this experiment is that the rate of hydrostatic tensile loading (or the tensile strain-rate) is difficult to control accurately, since this quantity depends both on the process of void growth and on the *local* hydrostatic tension (which cannot be measured directly). However, *Wu* et al. [33.111] have shown that a lower approxima-

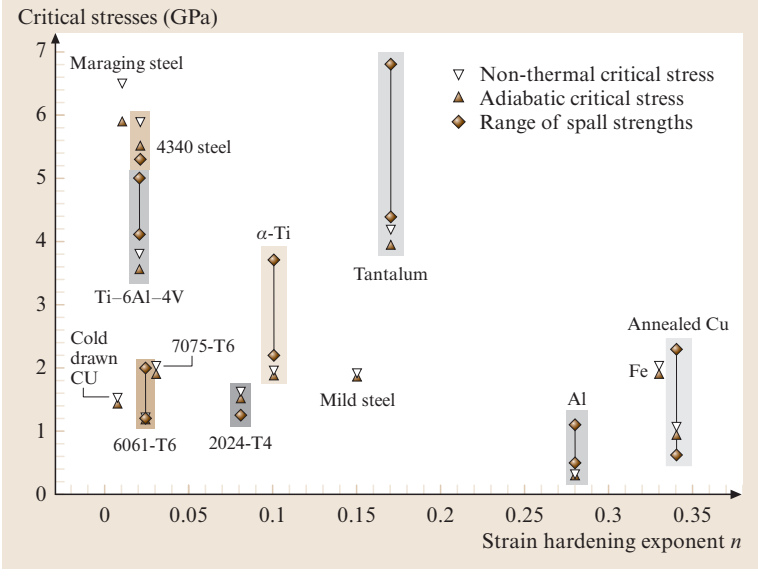

Fig. 33.22 Spall strength of a number of metals, as listed by *Wu* et al. [33.111]

tion to the spall strengths of most metals can be obtained using a critical pressure model.

33.4.2 Shear Band Experiments

The initiation and development of adiabatic shear bands in materials have been reviewed by *Bai* and *Dodd* [33.116] and more recently by *Wright* [33.117]. Adiabatic shear bands represent thermo-viscoplastic instabilities, and are often observed in ductile metals subjected to high rates of loading, because there is insufficient time to conduct away heat during the event. Such shear bands can be the dominant mode of failure in an impact event, and are particularly common in impacts involving ductile metals subjected to overall compression and also in the perforation and punching of sheets and plates. Adiabatic shear bands are also observed in applications such as high-speed machining, where they limit the speed of the manufacturing process.

The classical experimental technique used to study adiabatic shear bands is the dynamic torsion of thin-walled tubes in a torsional Kolsky bar experiment, as developed by *Marchand* and *Duffy* [33.48]. In this approach, an initially homogeneous torsional deformation of a thin-walled tube evolves into a strongly localized deformation with the development of an adiabatic shear band somewhere along the length of the tube during continued loading. Simultaneous recording of the stress history and the end displacement history together with time-resolved high-speed photography of the continuing deformation provides a direct measure of the time of occurrence of the adiabatic shear band. This technique has been used to study adiabatic shear band development in a variety of metals, including steel [33.118], Ti-6Al-4V [33.119] and tungsten heavy alloys [33.120]. Experiments of this type have guided much of the modeling that has been performed in the adiabatic shear band literature, since they can be considered to be simple shear experiments (at least until the onset of the instability). However, the technique has been shown to be extremely sensitive to defects in the dimensions of the specimen [33.121] and defects in the material, as with all dynamic failure processes.

To counter this, a predefined *defect* can be introduced into a thin-walled tube that is then subjected to dynamic torsion (not such experiments are essentially *designed* to study the failure process). Duffy and his coworkers introduced dimensional defects by hand using local polishing. *Deltort* [33.122] and *Chichili* and *Ramesh* [33.123] introduced standardized notches as defects in known locations using machining. *Chichili* and *Ramesh* [33.124] also developed a recovery technique, which allowed the recovery of specimens within which an adiabatic shear band had been grown under a single known torsional pulse, with a superimposed hydrostatic compressive load. A similar capability has been developed by *Bai* and co-workers [33.125]. Such approaches are critical for the development of an understanding of the deformation mechanisms [33.123] associated with adiabatic shear bands under well-defined dynamic loads.

A number of other experimental techniques have been developed, in which the emphasis is on the development of adiabatic shear bands in a repeatable manner so that the deformation micromechanisms can be studied. These include *hat* specimens deformed in a compression Kolsky bar [33.126], dynamic perforation or punching experiments [33.127], explosive loading [33.128] and *shear compression susceptibility* experiments [33.129]. A very interesting approach is to consider the asymmetric impact of prenotched plates [33.130]. In all of these cases, the simultaneous use of high-speed photography is a great asset. Further, given that the temperature is a critical component of the thermoviscoplastic problem, direct dynamic measurements of the temperature of the shear band tip are of great interest [33.131]. Unfortunately, a complete characterization of the deformation state and temperature state at the shear band tip continues to be difficult, and is an area of continuing research.

33.4.3 Expanding Ring Experiments

The tensile instability that is analogous to shear band development is the onset and growth of necking. However, the dynamic measurement of the necking instability is very difficult. The difficulties that arise are identical to the difficulties described in the high rate tension experiment earlier in this chapter: the end conditions required to develop the tension typically modify the failure mode. The most effective way to generate tension and study the necking instability is to use an expanding ring experiment. The dynamic expansion of the ring produces an initially axisymmetric tension mode, and the onset of the necking instability represents the breakage of symmetry within the experiment. There are three fundamental approaches to developing dynamic expansion of rings. The first is to use an explosive expansion, the second to use an electromagnetically driven expansion, and the third to use the axial motion of a wedge to develop a radial ex-

pansion of an enclosing ring. In practice, the first and third approaches are very difficult to control. Thus the primary experimental method available for expanding rings is that of electromagnetic launch [33.132–137]. This approach is often used to examine the development of tensile fragmentation in metallic systems, and has recently been coupled with high-speed photography to provide unprecedented detail of the dynamic necking process [33.138]. Although these experiments are extremely difficult to perform, the analysis of such experiments is very attractive to the theoretician and has the benefit of providing a great deal of insight (a recent analysis is presented by *Zhou* et al. [33.139] for the brittle case and by *Guduru* and *Freund* [33.140] for the ductile case). Related experiments involve explosive loading to generate expanding cylinders [33.141].

33.4.4 Dynamic Fracture Experiments

We do not discuss experimental techniques for dynamic fracture in any detail, since this topic is heavily discussed in the literature [33.142–146] and there is a very recent book on the subject [33.94]. Unlike quasi static fracture testing, dynamic fracture testing does not have an accepted set of testing standards. Thus there are a wide variety of specimen geometries, constraints, and loading conditions in use [33.94]. Most of these have in common the generation of a pre-fatigued crack and an attempt to measure the K-dominated crack-tip stress, strain or deformation fields, typically using optical diagnostics and/or high-speed photography. The specimens are often impulsively loaded using a Kolsky bar type configuration, or by direct impact in either 3-point bend, 1-point bend or asymmetric impact configurations (the Kalthoff experiment [33.147]). Useful results can also be obtained with crack opening measurements and properly located strain gauges [33.148], but it can be extremely difficult to identify the onset of crack propagation from the signals. The more commonly used optical diagnostics include photoelasticity [33.149], caustics [33.150], dynamic moiré [33.151], and coherent gradient sensing [33.152].

33.4.5 Charpy Impact Testing

Relatively rapid measures of the dynamic toughness of a material can be obtained using the ASTM standard Charpy impact test (ASTM E23-06). The technique essentially uses a notched bar for a specimen and a pendulum machine as an impacting device. Commercial pendulum machines are available to perform such experiments. There is also a NIST recommended guide for maintaining Charpy impact machines, NIST Special Publication 960-4. Versions of these devices have been developed for subscale testing, as well as for the testing of polymers. A recent reference book on pendulum impact machines has also been published by ASTM [33.153].

33.5 Further Reading

- Antounauthor]Please check the authors name., G.I. Kanel: *Spall Fracture* (Springer, New York 2004)
- Y.L. Bai, B. Dodd: *Adiabatic Shear Localization: Occurrence, Theories and Applications* (Pergamon, Oxford 1992)
- D.S. Drumheller: *Introduction to Wave Propagation in Nonlinear Fluids and Solids* (Cambridge Univ. Press, Cambridge 1998)
- J.E. Field, : Review of experimental techniques for high rate deformation and shock studies, Int. J. Imp. Eng. **30**, 725–775 (2004)
- G.T. Gray III: Classic Split-Hopkinson pressure bar testing. In: *ASM Handbook*, Vol. 8, ed. by H. Kuhn, D. Medlin, (ASM Int., Materials Park Ohio 2000) pp. 462–476
- K.A. Hartley, J. Duffy, R.H. Hawley: The torsional Kolsky (Split-Hopkinson) bar. In: *ASM Handbook*, Vol. 8, ed. by H. Kuhn, D. Medlin, (ASM Int., Materials Park Ohio 1985) pp. 218–228
- R.W. Klopp, R.J. Clifton: Pressure-shear plate impact testing. In: *ASM Handbook*, Vol. 8, ed. by H. Kuhn, D. Medlin, (ASM Int., Materials Park Ohio 1985) pp. 230–239
- M.A. Meyers: *Dynamic Behavior of Materials* (Wiley Interscience, New York 1994)
- T. Nicholas, A.M. Rajendran: Material characterization at high strain-rates. In: *High Velocity Impact Dynamics*, ed. by J.A. Zukas 1990, (Wiley, New York 1990) pp. 127–296
- K. Ravi-Chandar: *Dynamic Fracture* (Elsevier, Amsterdam 2004)
- T.W. Wright: *The Mathematical Theory of Adiabatic Shear Bands* (Cambridge Univ. Press, Cambridge 2002)

References

33.1 J.E. Field, : Review of experimental techniques for high rate deformation and shock studies, Int. J. Imp. Eng. **30**, 725–775 (2004)

33.2 C.S. Coffey, V.F. DeVost: Drop weight impact machines: a review of recent progress, JANNAF Propulsion Systems Hazards Subcommittee Meeting CPIA Publ., **1**(446), 527–531 (1986)

33.3 J.D. Winkel, D.F. Adams: Instrumented drop weight impact testing of cross-ply and fabric composites, Composites **16**(4), 268–278 (1985)

33.4 N. Banthia, : Impact testing of concrete using a drop-weight impact machine, Exp. Mech. **29**(1), 63–69 (1989)

33.5 P.R. Sreenivasan, : Determination of K(Id) at or below NDTT using instrumented drop-weight testing, Int. J. Fract. **55**(3), 273–283 (1992)

33.6 C.S. Coffey, V.F. Devost: Impact testing of explosives and propellants, Propellants Explosives Pyrotechnics **20**(3), 105–115 (1995)

33.7 H.M. Hsiao, I.M. Daniel, R.D. Cordes: Dynamic compressive behavior of thick composite materials, Exp. Mech. **38**(3), 172–180 (1998)

33.8 T. Nicholas, A.M. Rajendran: Material characterization at high strain-rates. In: *High Velocity Impact Dynamics*, ed. by J.A. Zukas (Wiley, New York 1990) pp. 127–296

33.9 S.M. Walley, J.E. Field: Strain rate sensitivity of polymers in compression from low to high strain rates, DYMAT J. **1**, 211–228 (1994)

33.10 G. Ravichandran, G. Subhash: A micromechanical model for high strain rate behavior of ceramics, Int. J. Sol. Struct. **32**, 2627–2646 (1995)

33.11 D. Jia, K.T. Ramesh, E. Ma: Effects of nanocrystalline and ultrafine grain sizes on constitutive behavior and shear bands in iron, Acta Mater. **51**(12), 3495–3509 (2003)

33.12 H. Kolsky: An investigation of the mechanical properties of materials at very high rates of loading, Proceedings of the Physical Society, Vol. 62B (London, 1949) p. 676

33.13 G.T. Gray III: Classic split-Hopkinson pressure bar testing. In: *ASM Handbook*, Vol. 8, ed. by H. Kuhn, D. Medlin (ASM Int., Materials Park Ohio 2000) pp. 462–476

33.14 K.T. Ramesh, S. Narasimhan: Finite deformations and the dynamic measurement of radial strains in compression Kolsky bar experiments, Int. J. Sol. Struct. **33**(20), 3723–3738 (1996)

33.15 T.S. Lok, : Testing and response of large diameter brittle materials subjected to high strain rate, J. Mat. Civil Eng. **14**(3), 262–269 (2002)

33.16 D. Jia, K.T. Ramesh: A rigorous assessment of the benefits of miniaturization in the Kolsky bar system, Exp. Mech. **44**(5), 445–454 (2004)

33.17 E.D.H. Davies, S.C. Hunter: The dynamic compression testing of solids by the method of the split Hopkinson pressure bar (SHPB), J. Mech. Phys. Solids **11**, 155–179 (1963)

33.18 J.F. Bell: An experimental diffraction grating study of the quasi-static hypothesis of the SHPB experiment, J. Mech. Phys. Solids **14**, 309–327 (1966)

33.19 L.D. Bertholf, C.H. Karnes: Two dimensional analysis of the split Hopkinson pressure bar system, J. Mech. Phys. Solids **23**, 1–19 (1975)

33.20 A.S.E., : *Standard test method of compression testing of metallic at room temperature* (pub]Please add the publisher., place]Please add the place of publishing. 1999)

33.21 F. Wang, J.G. Lenard: An experimental study of interfacial friction-hot ring compression, Trans. ASME: J. Eng. Mater. Technol. **114**, 13–18 (1992)

33.22 R. Skalak: Longitudinal impact of a semi-infinite circular elastic bar, J. Appl. Mech. **24**, 59–64 (1957)

33.23 D.J. Frew, M.J. Forrestal, W. Chen: Pulse shaping techniques for testing brittle materials with a split Hopkinson pressure bar, Exper. Mech. **42**, 93–106 (2002)

33.24 D.A. Gorham: Specimen inertia in high strain-rate compression, J. Phys. D **22**, 1888–1893 (1989)

33.25 J.Z. Malinowski, J.R. Klepaczko: A unified analytic and numerical approach to specimen behaviour in the SHPB, Int. J. Mech. Sci. **28**, 381–391 (1986)

33.26 G. Subhash, G. Ravichandran: Split-Hopkinson bar testing of ceramics. In: *ASM Handbook*, Vol. 8, ed. by H. Kuhn, D. Medlin, (ASM Int., Materials Park Ohio 2000) pp. 497–504

33.27 H. Wang, K.T. Ramesh: Dynamic strength and fragmentation of hot-pressed silicon carbide under uniaxial compression, Acta mater. **52**(2), 355–367 (2004)

33.28 G. Subhash, G. Ravichandran: Mechanical behaviour of a hot pressed aluminum nitride under uniaxial compression, J. Mater. Sci. **33**, 1933–1939 (1998)

33.29 G. Ravichandran, G. Subhash: Critical appraisal of limiting strain rates for compression testing of ceramics in a split Hopkinson pressure bar, J. Amer. Ceram. Soc. **77**, 263–267 (1994)

33.30 W. Chen, G. Subhash, G. Ravichandran: Evaluation of ceramic specimen geometries used in split Hopkinson pressure bar, DYMAT J. **1**, 193–210 (1994)

33.31 W. Chen, : Dynamic compression testing of soft materials, Trans. ASME: J. Appl. Mech. **69**, 214–223 (2002)

33.32 G.T. Gray III, W.R. Blumenthal: Split-Hopkinson pressure bar testing of soft materials. In: *ASM Handbook*, Vol. 8, ed. by H. Kuhn, D. Medlin, (ASM Int., Materials Park Ohio 2000) pp. 462–476

33.33 C.R. Siviour, : Are low impedance Hopkinson bars necessary for stress equilibrium in soft materials?. In: *New Experimental Methods in Material Dynamics and Impact*, ed. by W.K. Nowacki, J.R. Klepaczko (Inst. Fund. Technol. Res., Warsaw 2001) pp. 421–427

33.34 W. Chen, F. Lu, B. Zhou: A quartz-crystal-embedded split Hopkinson pressure bar for soft materials, Exper. Mech. **40**, 1–6 (2000)

33.35 D.T. Casem, W. Fourney, P. Chang: Wave separation in viscoelastic pressure bars using single-point measurements of strain and velocity, Polymer Testing **22**, 155–164 (2003)

33.36 J.L. Chiddister, L.E. Malvern: Compression-impact testing of aluminum at elevated temperatures, Exper. Mech. **3**, 81–90 (1963)

33.37 Z. Rosenberg, : A new technique for heating specimens in Split-Hopkinson-bar experiments using induction coil heaters, Exper. Mech. **26**, 275–278 (1986)

33.38 A. Gilat, X. Wu: Elevated temperature testing with the torsional split Hopkinson bar, Exper. Mech. **34**, 166–170 (1994)

33.39 A.M. Lennon, K.T. Ramesh: A technique for measuring the dynamic behavior of materials at high temperatures, Int. J. Plast. **14**(12), 1279–1292 (1998)

33.40 S. Nemat-Nasser, J.B. Isaacs: Direct Measurement of Isothermal Flow Stress of Metals at Elevated Temperature and High Strain Rates with Application to Ta and Ta-W Alloys, Acta Mater. **45**(3), 907–919 (1997)

33.41 D. Basak, : Temperature control of pulse heated specimens in a Kolsky bar apparatus using microsecond time-resolved pyrometry, Int. J. Thermophys. **25**(2), 561–574 (2004)

33.42 J. Harding, E.O. Wood, J.D. Campbell: Tensile testing of materials at impact rates of strain, J. Mech. Engng Sci. **2**, 88–96 (1960)

33.43 S. Nemat-Nasser, J.B. Isaacs, J.E. Starrett: Hopkinson techniques for dynamic recovery experiments, Proc. Royal Soc. London **A20**, 371–391 (1991)

33.44 G.H. Staab, A. Gilat: A direct-tension split Hopkinson bar for high strain-rate testing, Exp. Mech. **31**(3), 232–235 (1991)

33.45 Y. Li, K.T. Ramesh, E.S.C. Chin: Comparison of the plastic deformation and failure of A359/SiC and 6061-T6/Al203 metal matrix composites under dynamic tension, Mat. Sci. Eng. A **371**(1-2), 359–370 (2004)

33.46 W.E. Baker, C.H. Yew: Strain-rate effects in the propagation of torsional plastic waves, Trans. ASME: J. Appl. Mech. **33**, 917–923 (1966)

33.47 K.A. Hartley, J. Duffy, R.H. Hawley: The torsional Kolsky (split-Hopkinson) bar. In: *ASM Handbook*, Vol. 8, ed. by H. Kuhn, D. Medlin, (ASM Int., Materials Park Ohio 2000) pp. 218–228

33.48 A. Marchand, J. Duffy: An experimental study of the formation process of adiabatic shear bands in a structural steel, J. Mech. Phys. Solids. **36**(3), 251–283 (1988)

33.49 C.K.H. Dharan, F.E. Hauser: Determination of stress-strain characteristics at very high strain rates, Exper. Mech. **10**, 370–376 (1970)

33.50 G.L. Wulf, G.T. Richardson: The measurement of dynamic stress-strain relationships at very high strain rates, J. Phys. E **7**, 167–169 (1974)

33.51 D.A. Gorham: Measurement of stress-strain properties of strong metals at very high strain rates, Inst. Phys. Conf. Ser. **47**, 16–24 (1980)

33.52 N.A. Safford: Materials testing up to $10^5 s^{-1}$ using a miniaturised hopkinson bar with dispersion corrections, Proc. 2nd Intl. Symp. on Intense Dynamic Loading and its Effects, ed. by G. Zhang, S. Huang (Sichuan Univ. Press, Chengdu 1992) pp. 378–383

33.53 D.A. Gorham, P.H. Pope, J.E. Field: An improved method for compressive stress-strain measurements at very high strain rates, Proc. R. Soc. Lond. A **438**, 153–170 (1992)

33.54 J. Shioiri, K. Sakino, S. Santoh: Strain rate sensitivity of flow stress at very high rates of strain. In: *Constitutive Relation in High/Very-High Strain Rates*, ed. by K. Kawata, J. Shioiri (Springer, Berlin Heidelberg 1995) pp. 49–58

33.55 F. Kamler, P. Niessen, R.J. Pick: Measurement of the behaviour of high-purity copper at very high rates of strain, Canad. J. Phys. **73**, 295–303 (1995)

33.56 R.W. Klopp, R.J. Clifton: Pressure-shear plate impact testing. In: *ASM Handbook*, Vol. 8, ed. by H. Kuhn, D. Medlin, (ASM Int., Materials Park Ohio 1985) pp. 230–239

33.57 K.J. Frutschy, R.J. Clifton: High-temperature pressure-shear plate impact experiments on OFHC copper, J. Mech. Phys. Sol. **46**(10), 1723–1743 (1998)

33.58 K.T. Ramesh, N. Kelkar: Technique for the continuous measurement of projectile velocities in plate impact experiments, Rev. Sci. Instrum. **66**(4), 3034–3036 (1995)

33.59 S. Yadav, D.R. Chichili, K.T. Ramesh: The mechanical response of a 6061-T6 Al/Al_2O_3 metal matrix composite at high rates of deformation, Acta metall. mater. **43**(12), 4453–4464 (1995)

33.60 D. Jia, A.M. Lennon, K.T. Ramesh: High-strain-rate pressure-shear recovery: a new experimental technique, Int. J. Sol. Struc. **37**(12), 1679–1699 (2000)

33.61 A. Bekker : Impact induced propagation of phase transformation in a shape memory alloy rod, Int. J. Plast. **18**, 1447–1479 (2002)

33.62 J.U. Cazamias, : Bar impact tests on alumina (AD995). In: *Shock Compression of Condensed Matter – 2001*, ed. by M.D. Furnish, N.N. Thadhani, Y. Horie (Am. Inst. Phys., Melville 2002) pp. 787–790

33.63 L.C. Chhabildas, : Impact of AD995 alumina rods. In: *Shock Compression of Condensed Matter – 1997*, ed. by S.C. Schmidt, D.P. Dandekar, J.W. Forbes (Am. Inst. Phys., Woodbury 1998) pp. 505–508

33.64 F.G. Díaz-Rubio, J. Rodríguez Pérez, V. Sánchez Gálvez: The spalling of long bars as a reliable method of measuring the dynamic tensile strength of ceramics, Int. J. Impact Eng. **27**, 161–177 (2002)

33.65 K.G. Holland, : Experiments on CERCOM SiC rods under impact. In: *Shock Compression of Condensed Matter – 1999*, ed. by M.D. Furnish, L.C. Chhabildas, R.S. Hixson (Am. Inst. Phys., Melville 2000) pp. 585–588

33.66 R. Russell, S.J. Bless, T. Beno: Impact induced failure zones in Homalite bars:. In: *Shock Compression of Condensed Matter – 2001*, ed. by M.D. Furnish, N.N. Thadhani, Y. Horie, (Am. Inst. Phys., Melville 2002) pp. 811–814

33.67 D.S. Drumheller: *Introduction to Wave Propagation in Nonlinear Fluids and Solids* (Cambridge Univ. Press, Cambridge 1998)

33.68 M.A. Meyers: *Dynamic Behavior of Materials* (Wiley, New York 1994)

33.69 G.T. Gray III: Shock wave testing of ductile materials. In: *ASM Handbook*, Vol. 8, ed. by H. Kuhn, D. Medlin, (ASM Int., Materials Park Ohio 2000) pp. 462–476

33.70 S.C. Schmidt, J.N. Johnson, L.W. Davidson: *Shock Compression of Condensed Matter – 1989* (North Holland, Amsterdam 1990)

33.71 S.C. Schmidt, : *Shock Compression of Condensed Matter – 1991* (Elsevier, Amsterdam 1992)

33.72 S.C. Schmidt, W.C. Tao: *Shock Compression of Condensed Matter – 1995* (Am. Inst. Phys., Woodbury 1996)

33.73 S.C.D.P. Schmidt Dandekar, J.W. Forbes: *Shock Compression of Condensed Matter – 1997* (Am. Inst. Phys., Woodbury 1998)

33.74 M.D. Furnish, L.C. Chhabildas, R.S. Hixson: *Shock Compression of Condensed Matter – 1999* (Am. Inst. Phys., Melville 2000)

33.75 L. Davison, R.A. Graham: Shock compression of solids, Phys. Rep. **55**, 255–379 (1979)

33.76 J.R. Asay, M. Shahinpoor: *High-Pressure Shock Compression of Solids* (Springer-Verlag, New York 1993)

33.77 L. Davison, D.E. Grady, M. Shahinpoor: *High-Pressure Shock Compression of Solids II: Dynamic Fracture and Fragmentation* (Springer, New York 1996)

33.78 L. Davison, Y. Horie, M. Shahinpoor: *High-Pressure Shock Compression of Solids IV: Response of Highly Porous Solids to Shock Compression* (Springer, New York 1997)

33.79 L. Davison, M. Shahinpoor: *High-Pressure Shock Compression of Solids III* (Springer, New York 1998)

33.80 H. Czichos, T. Saito, L. Smith (Eds.): *Springer Handbook of Materials Measurement Methods* (Springer, Berlin, Heidelberg 2006)

33.81 W.D. Reinhart, : Equation of state measurements of materials using a three-stage gun to impact velocities of 11 km/s, Int. J. Imp. Eng. **26**(1-10), 625–637 (2001)

33.82 Y.M. Gupta: Use of piezoresistance gauges to quantify the stress state in a shocked solid. In: *Experimental Techniques in the Dynamics of Deformable Solids*, ed. by K.T. Ramesh (ASME, New York 1993) pp. 89–101

33.83 R. Feng, G.F. Raiser, Y.M. Gupta: Material strength and inelastic deformation of silicon carbide under shock wave compression, J. Appl. Phys. **83**(1), 79–86 (1998)

33.84 Z. Rosenberg, D. Yaziv, Y. Partom: Calibration of foil-like manganin gauges in planar shock-wave experiments, J. Appl. Phys. **51**(6), 3702–3705 (1980)

33.85 Y.M. Gupta: Analysis of manganin and ytterbium gauge data under shock loading, J. Appl. Phys. **54**(9), 6094–6098 (1983)

33.86 R.A. Graham, F.W. Neilson, W.B. Benedick: Piezoelectric current from shock-loaded quartz – a submicrosecond stress gauge, J. Appl. Phys. **36**(5), 1775–00 (1965)

33.87 T. Obara, N.K. Bourne, Y. Mebar: The construction and calibration of an inexpensive PVDF stress gauge for fast pressure measurements, Meas. Sci. Technol. **6**(4), 345–348 (1995)

33.88 L.M. Barker: The accuracy of VISAR instrumentation. In: *Shock Compression of Condensed Matter – 1997*, ed. by S.C. Schmidt, D.P. Dandekar, J.W. Forbes (Am. Inst. Phys., Woodbury, 1998) pp. 833–836

33.89 L.M. Barker: The development of the VISAR and its use in shock compression science. In: *Shock Compression of Condensed Matter – 1999*, ed. by M.D. Furnish, L.C. Chhabildas, R.S. Hixson, (Am. Inst. Phys., Melville 2000) pp. 11–17

33.90 L.M. Barker, R.E. Hollenbach: Laser interferometer for measuring high velocities of any reflecting surface, J. Appl. Phys. **43**, 4669–4675 (1972)

33.91 J. Edwards, : Laser-driven plasma loader for shockless compression and acceleration of samples in the solid state, Phys. Rev. Let. **92**(6), 000–000 (2004)

33.92 N.K. Bourne, Z. Rosenberg, J.E. Field: High-speed photography of compressive failure waves in glasses, J. Appl. Phys. **78**, 3736–3739 (1995)

33.93 B. Paliwal, K.T. Ramesh, J.W. McCauley: Direct observation of the dynamic compressive failure of a transparent polycrystalline ceramic (AlON), J. Am. Ceramic Soc. **89**(6), 2128–2133 (2006)

33.94 K. Ravi-Chandar: *Dynamic fracture* (Wiley, New York 2005)

33.95 E. El-Magd, M. Brodmann: Influence of precipitates on ductile fracture of aluminium alloy AA7075 at high strain rates, Mat. Sci. Eng. A. Struct. Mat. Prop. Microstruct. Proces. **307**(1-2), 143–150 (2001)

33.96 D.M. Goto, D.A. Koss, V. Jablokov: The influence of tensile stress states on the failure of HY-100 steel, Metallurg. Mat. Trans. A **30**(9), 2835–2842 (1999)

33.97 J. Kang, : Microscopic strain mapping using scanning electron microscopy topography image correlation at large strain, J. Strain Anal. Eng. Design **40**(5), 559–570 (2005)

33.98 W. Tong, : Deformation and fracture of miniature tensile bars with resistance-spot-weld microstructures, Metallurg. Mat. Trans. A **36A**(10), 2651–2669 (2005)

33.99 B. Wattrisse, : Kinematic manifestations of localisation phenomena in steels by digital image correlation, Europ. J. Mech. A **20**(2), 189–211 (2001)

33.100 B. Wattrisse, : Analysis of strain localization during tensile tests by digital image correlation, Exp. Mech. **41**(1), 29–39 (2001)

33.101 P.E. Magnusen, E.M. Dubensky, D.A. Koss: The effect of void arrays on void linking during ductile fracture, Acta Metallurgica **36**(5), 1503–1509 (1988)

33.102 E.M. Dubensky, D.A. Koss: Void pore distributions and ductile fracture, Metallurg. Mat. Trans. A **18**(9), 1887–1895 (1987)

33.103 R.J. Bourcier, : The influence of porosity on the deformation and fracture of alloys, Acta Metallurgica **34**(12), 2443–2453 (1986)

33.104 T. Pardoen, I. Doghri, F. Delannay: Experimental and numerical comparison of void growth models and void coalescence criteria for the prediction of ductile fracture in copper bars, Acta Mater. **46**(2), 541–00 (1998)

33.105 W.G. Proud: X-ray. In: *Shock Compression of Condensed Matter*, ed. by ed]Please add the editor. (AIP, Baltimore 2005)

33.106 G. Ravichandran, R.J. Clifton: Dynamic fracture under plane-wave loading, Int. J. Fract. **40**(3), 157–201 (1989)

33.107 V. Prakash, L.B. Freund, R.J. Clifton: Stress wave radiation from a crack tip during dynamic initiation, J. Appl. Mech.-Trans. ASME **59**(2), 356–365 (1992)

33.108 M. Zhou, R.J. Clifton: Dynamic ductile rupture under conditions of plane strain, Int. J. Imp. Eng. **19**(3), 189–206 (1997)

33.109 Z. Zhang, R.J. Clifton: Shear band propagation from a crack tip, J. Mech. Phys Sol. **51**(11-12), 1903–1922 (2003)

33.110 R. Godse, G. Ravichandran, R.J. Clifton: Micromechanisms of dynamic crack-propagation in an aisi-4340-steel, Mat. Sci. Eng. A **112**, 79–88 (1989)

33.111 X.Y. Wu, K.T. Ramesh, T.W. Wright: The effects of thermal softening and heat conduction on the dynamic growth of voids, Int. J. Sol. Struct. **40**(13), 4461–4478 (2003)

33.112 J.N. Johnson: Dynamic fracture and spallation in ductile solids, J. Appl. Phys. **52**(4), 2812–2825 (1981)

33.113 D.E. Grady: The spall strength of condensed matter, J. Mech. Phys Sol. **36**(3), 353–00 (1988)

33.114 G.I. Kanel, : Dynamic yield and tensile strength of aluminum single crystals at temperatures up to the melting point, J. Appl. Phys. **90**(1), 136–143 (2001)

33.115 Antoun , G.I. Kanel: *Spall Fracture* (Springer, Berlin Heidelberg 2004)

33.116 Y.L. Bai, B. Dodd: *Adiabatic Shear Localization: Occurrence, Theories and Applications* (Pergamon, Oxford 1992)

33.117 T.W. Wright: *The mathematical theory of adiabatic shear bands* (Cambridge Univ. Press, Cambridge 2002)

33.118 J.H. Giovanola: Observation of adiabatic shear banding in simple torsion. In: *Impact Loading and Dynamic Behaviour of Materials*, ed. by C.Y. Chiem, H.D. Kunze, L.W. Meyer (DGM Informationsgesellschaft, Oberursel 1988) pp. 705–710

33.119 M.G. daSilva, K.T. Ramesh: The rate-dependent deformation and localization of fully dense and porous Ti-6Al-4V, Mat. Sci. Eng. A **232**(1-2), 11–22 (1997)

33.120 K.T. Ramesh: On the localization of shearing deformations in a tungsten heavy alloy, Mech. Materials **17**, 165–173 (1994)

33.121 A. Molinari, R.J. Clifton: Analytical characterization of shear localization in thermoviscoplastic materials, J. Appl. Mech.-Trans. ASME **54**(4), 806–812 (1987)

33.122 B. Deltort: Experimental and numerical aspects of adiabatic shear in a 4340 steel, J. Phys. IV France Colloq. C8 (DYMAT 94) **4**, 447–452 (1994)

33.123 D.R. Chichili, K.T. Ramesh, K.J. Hemker: Adiabatic shear localization in alpha-titanium: experiments, modeling and microstructural evolution, J. Mech. Phys Sol. **52**(7), 1889–1909 (2004)

33.124 D.R. Chichili, K.T. Ramesh: Recovery experiments for adiabatic shear localization: A novel experimental technique, J. Appl. Mech.-Transact. ASME **66**(1), 10–20 (1999)

33.125 Q. Xue, L.T. Shen, T.L. Bai: Elimination of loading reverberation in the split Hopkinson torsional bar, Rev. Sci. Instr. **66**(9), 5298–5304 (1995)

33.126 M.A. Meyers, : Evolution of microstructure and shear-band formation in alpha-hcp titanium, Mech. Mat. **17**(2-3), 175–193 (1994)

33.127 Z.Q. Duan, S.X. Li, D.W. Huang: Microstructures and adiabatic shear bands formed by ballistic impact in steels and tungsten alloy, Fat. Fract. Eng. Mat. Struct. **26**(12), 1119–1126 (2003)

33.128 Q. Xue, M.A. Meyers, V.F. Nesterenko: Self-organization of shear bands in titanium and Ti-6Al-4V alloy, Acta Mater. **50**(3), 575–596 (2002)

33.129 D. Rittel, S. Lee, G. Ravichandran: A shear-compression specimen for large strain testing, Exp. Mech. **42**(1), 58–64 (2002)

33.130 M. Zhou, A.J. Rosakis, G. Ravichandran: Dynamically propagating shear bands in impact-loaded prenotched plates. 1. Experimental investigations of temperature signatures and propagation speed, J. Mech. Phys Sol. **44**(5), 981–1006 (1996)

33.131 P.R. Guduru, A.J. Rosakis, G. Ravichandran: Dynamic shear bands: an investigation using high

speed optical and infrared diagnostics, Mech. Mat. **33**(6), 371–402 (2001)
33.132 D.E. Grady, D.A. Benson: Fragmentation of metal rings by electromagnetic loading, Exp. Mech. **23**(4), 393–400 (1983)
33.133 W.H. Gourdin: The expanding ring as a high-strain rate test, J. Met. **39**(10), A65–A65 (1987)
33.134 S. Dujardin, G. Gazeaud, A. Lichtenberger: Dynamic behavior of copper studied using the expanding ring test, J. Physique **49**(C-3), 55–62 (1988)
33.135 W.H. Gourdin: Analysis and assessment of electromagnetic ring expansion as a high-strain-rate test, J. Appl. Phys. **65**(2), 411–422 (1989)
33.136 W.H. Gourdin: Constitutive properties of copper and tantalum at high-rates of tensile strain – expanding ring results, Inst. Phys. Conf. Ser. **102**, 221–226 (1989)
33.137 W.H. Gourdin, S.L. Weinland, R.M. Boling: Development of the electromagnetically launched expanding ring as a high-strain-rate test technique, Rev. Sci. Instr. **60**(3), 427–432 (1989)
33.138 H. Zhang, K. Ravi-Chandar: *Dynamic necking of 6061-0 Aluminum* (, 2006), ed by K. T. Ramseh
33.139 F.H. Zhou, J.F. Molinari, K.T. Ramesh: Analysis of the brittle fragmentation of an expanding ring, Comp. Mat. Sci. **37**(1-2), 74–85 (2006)
33.140 P.R. Guduru, L.B. Freund: The dynamics of multiple neck formation and fragmentation in high rate extension of ductile materials, Int. J. Sol. Struct. **39**(21-22), 5615–5632 (2002)
33.141 M.J. Forrestal, B.W. Duggin, R.I. Butler: Explosive loading technique for the uniform expansion of 304 stainless steel cylinders at high strain rates, J. Appl. Mech.-Transact. ASME **47**(1), 17–20 (1980)
33.142 J.F. Kalthoff: On the measurement of dynamic fracture toughnesses – a review of recent work, Int. J. Fract. **27**(3-4), 277–298 (1985)
33.143 R.A.W. Mines: Characterization and measurement of the mode 1-dynamic initiation of cracks in metals at intermediate strain rates – a review, Int. J. Imp. Eng. **9**(4), 441–454 (1990)
33.144 A.J. Rosakis: Application of coherent gradient sensing (cgs) to the investigation of dynamic fracture problems, Optics Lasers Eng. **19**(1-3), 3–41 (1993)
33.145 K. Ravi-Chandar: Dynamic fracture of nominally brittle materials, Int. J. Fract. **90**(1-2), 83–102 (1998)
33.146 A. Shukla: High-speed fracture studies on bimaterial interfaces using photoelasticity – a review, J. Strain Anal. Eng. Design **36**(2), 119–142 (2001)
33.147 J.F. Kalthoff: Modes of dynamic shear failure in solids, Int. J. Fract. **101**(1-2), 1–31 (2000)
33.148 D.D. Anderson, A. Rosakis: Comparison of three real time techniques for the measurement of dynamic fracture initiation toughness in metals, Eng. Fract. Mech. **72**(4), 535–555 (2005)
33.149 V. Parameswaran, A. Shukla: Dynamic fracture of a functionally gradient material having discrete property variation, J. Mat. Sci. **33**(10), 3303–331 (1998)
33.150 A.J. Rosakis, A.T. Zehnder, R. Narasimhan: Caustics by reflection and their application to elastic-plastic and dynamic fracture-mechanics, Optic. Eng. **27**(7), 596–610 (1988)
33.151 K. Arakawa, : Dynamic fracture-analysis by moire interferometry, Exp. Mech. **31**(4), 306–309 (1991)
33.152 H.V. Tippur, A.J. Rosakis: Quasi-static and dynamic crack-growth along bimaterial interfaces – a note on crack-tip field-measurements using coherent gradient sensing, Exp. Mech. **31**(3), 243–251 (1991)
33.153 T.A. Siewert, M.P. Monahan: *Pendulum Impact Testing: A Century of Progress* (ASTM, 2000)
ocite]This reference is not cited in the text.
33.154 M.F. Gogulya, A.Y. Dolgoborodov, M.A. Brazhnikov: Investigation of shock and detonation waves by optical pyrometry, Int. J. Imp. Eng. **23**(1), 283–293 (1999)
33.155 G.I. Pangilinan, Y.M. Gupta: Time-resolved raman measurements in nitromethane shocked to 140 Kbar, J. Phys. Chem. **98**(13), 4522–4529 (1994)

http://www.springer.com/978-0-387-26883-5

Springer Handbook of Experimental Solid Mechanics
Sharpe, Jr., W.N. (Ed.)
2008, XXX, 1098 p., Hardcover
ISBN: 978-0-387-26883-5